AIAA AVIATION Forum
June 15-19, 2020, VIRTUAL EVENT
AIAA AVIATION 2020 FORUM

10.2514/6.2020-2994

Hypersonic Boundary-Layer Receptivity to a Freestream Entropy Pulse with Real-Gas and Nose Bluntness Effects

Anand R. Varma* and Xiaolin Zhong†
University of California, Los Angeles, California, 90095, USA

In hypersonic flows, temperatures can be high enough to induce significant thermal and chemical nonequilibrium effects. However, few numerical studies on hypersonic boundary-layer receptivity have incorporated such real-gas effects. In this study, thermochemical nonequilibrium Direct Numerical Simulation (DNS) and Linear Stability Theory (LST) was used to investigate the boundary-layer receptivity of a 5-degree half-angle circular cone at Mach 5 to a freestream planar entropy pulse. Computations were performed for two cases with nose radii of 1 mm and 25 mm respectively. In the 1 mm nose radius case, LST predicted mode F1 to be the second mode with a large unstable supersonic mode region. The combined results of DNS and LST suggest that fast acoustic waves generated by the interaction of the planar entropy pulse with the shock excited the second mode. In the 25 mm nose radius case, preliminary DNS results did not indicate an unstable second mode region, but featured small regions of growth upstream likely due to forcing by waves generated by the shock-disturbance interaction. The second mode region in the 25 mm nose radius case is expected to occur further downstream.

I. Introduction

Turbulent flow is associated with a substantial increase in heat fluxes and skin drag for hypersonic vehicles compared to a laminar flow. Historically this issue has posed significant challenges to hypersonic vehicle design. For example, excessive heating requires the use of heavy thermal protection systems which may negatively impact aerodynamic characteristics. If laminar-to-turbulent transition can be predicted and delayed, the performance of vehicles in extended hypersonic flight can be improved.

In hypersonic boundary-layers, initially small disturbances can be destabilized and eventually lead to laminar-to-turbulent transition. These disturbances are a combination of acoustic, entropy and vorticity waves. Each type of disturbance can further be divided into discrete and continuous modes. The eigenfunctions associated with discrete modes decay into the freestream, whereas the eigenfunctions associated with continuous modes do not. The two types of discrete modes of interest here are the fast and slow acoustic modes, named as such because they originate from the fast and slow acoustic continuous spectrum respectively. Following the terminology of Fedorov and Tumin,[1] the series of fast acoustic discrete modes are called mode F1, F2, F3 and so on whereas the slow acoustic discrete mode is called mode S. The second mode instability arises when Mode F1 synchronizes with Mode S. During this synchronization, one of the two modes is destabilized. The unstable mode is referred to as the second mode. In recent years there has been interest in a lesser-known instability referred to as the supersonic mode due to its existence in some high-enthalpy ground facilities, such as the T5 tunnel at Caltech. The supersonic mode travels upstream supersonically relative to the meanflow outside of the boundary layer and is associated with acoustic-like waves emanating into the freestream. Knisely and Zhong[2,3] proposed that these waves originate from a resonant trimodal interaction between mode F1, mode S and the slow acoustic continuous spectrum and may not be able to be captured by LST in certain scenarios. As a result, the supersonic mode can be more difficult to predict. Overall, a full understanding of the supersonic mode and the conditions in which it exists requires further research.

*Ph.D. Student, Mechanical and Aerospace Engineering, varmaar@ucla.edu, AIAA Student Member.
†Professor, Mechanical and Aerospace Engineering, xiaolin@seas.ucla.edu, AIAA Associate Fellow.

In a low-disturbance environment, boundary-layer disturbances can be created when freestream disturbances enter the shock and generate disturbance waves within the shock layer. This process is referred to as receptivity. In ground tests, fast and slow acoustic disturbances are typically more dominant whereas in flight conditions, entropy and vorticity disturbances are more dominant. Upon interacting with the shock, disturbances will generate all four types of waves.[4] The acoustic waves are somewhat unique in that they can reflect off of the wall and re-interact with the shock, generating further disturbances.[5,6] After propagating downstream, these disturbances can then excite the second mode through direct interaction or through the excitation of the stable discrete mode which then exchanges energy with the second mode.

Hypersonic boundary layer receptivity has been studied extensively over the years. Ma and Zhong[5–7] performed a comprehensive DNS study of the receptivity of Mach 4.5 flow over a flat plate to a variety of freestream disturbances. They found that the receptivity process for freestream fast acoustic, entropy and vorticity disturbances was similar in that these waves do not directly interact with the second mode. Rather, they excite a stable mode F1 which then synchronizes with mode S to destabilize the second mode. On the other hand, slow acoustic disturbances can directly interact with mode S, leading to significantly higher disturbance amplitudes than the former. Balakumar and Kegerise[8] performed a DNS study of the receptivity of a Mach 6 flow over a cone to acoustic and vorticity disturbances and found that boundary-layer disturbances are more receptive to slow acoustic waves than fast acoustic waves. In addition, they found that although vorticity waves excited the second mode indirectly through the fast acoustic discrete mode. Fedorov *et al.*[9] performed a DNS study of the receptivity of a Mach 6 flow over a flat plate to temperature spots. They found that if temperature spots imposed outside of the shock, the shock-disturbance interaction generated acoustic waves which directly excited the second mode. Huang and Zhong[10] studied the receptivity of a Mach 6 compression cone to spherical entropy hotspots modeled as Gaussian temperature pulses. They found that an entropy hotspot excited the second mode through the generation of fast acoustic waves in the nose region. They were also able to estimate receptivity coefficients for the second mode from unsteady DNS by normalizing the overall disturbance amplitude by the LST-derived N-factors at that location. Recently, He and Zhong[11] studied the receptivity of a Mach 10 blunt cone flow at zero angle of attack using a variety of acoustic, entropy and vorticity pulses. They found that while all of the disturbances can excite the second mode, the slow acoustic pulse had the highest receptivity coefficients. Its worth noting that in all of these studies, mode S was the second mode. In the current study, mode F1 is the unstable mode and the receptivity mechanism may be quite different. In addition, the above studies were focused primarily on perfect-gas flows.

Real flight vehicles may also have blunted noses to reduce surface heat fluxes. However, the question of the nose bluntness effect on boundary-layer stability has pervaded hypersonics research for a number of years. Experimental studies by Stetson[12] found that moderate nose bluntness moves the transition location downstream. However, when the nose radius is increased further, it can cause the transition location to move upstream. The many numerical studies undertaken in this area since then have not found evidence of this transition reversal. In fact, some researchers found the opposite result. For example, Malik *et al.*[13] found that nose bluntness damped second-mode disturbances. Lei and Zhong[14] performed a joint DNS/LST study of Stetson's Mach 5.5 experiments found that nose bluntness always delays the onset of second-mode instabilities. Kara *et al.*[15] studied the effect of nose bluntness on the receptivity of a blunt cone at Mach 6 to freestream planar slow acoustic waves and found that receptivity coefficients decreased by over 10^3 for a blunt nose compared to a sharp nose.

In-flight conditions and some ground tests may experience very high temperatures such that real-gas effects, such as chemical and vibrational nonequilibrium, will be significant. Numerical studies by Malik,[16] Chang *et al.*,[17] Johnson *et al.*[18–20] and Hudson *et al.*[21] found that the dissociation of air species can destabilize the second mode. A recent study by Mortensen[22] has found that for a Mach 20 real-gas flow, sufficiently large nose bluntness can destabilize the supersonic mode. Although he found that nose bluntness reduced the growth rate of the supersonic mode, the unstable supersonic region was simultaneously lengthened and shifted upstream relative to the second mode region. The combination of these two factors meant that the supersonic mode could attain transition N-factors earlier than the second mode. Mortensen found that the destabilization of the supersonic mode was due to the increased recombination of atomic oxygen within the boundary. Recently, Knisely and Zhong[23] have shown that thermal nonequilibrium has a stabilizing effect on the second and supersonic modes.

Few receptivity studies have incorporated real-gas effects. Ma and Zhong[24] performed a numerical study of receptivity for a Mach 10 reacting oxygen flow over a flat plate to freestream planar acoustic disturbances. They found that thermochemical nonequilibrium was destabilizing; the peak amplitude was larger and the

second mode unstable region was extended. Parsons and Zhong[25] studied the receptivity of Mach 15.3 flow over a blunt cone to freestream acoustic disturbances. Using a 5-species gas model (as will be done in the current study), they determined that thermochemical nonequilibrium led to greater perturbation amplitudes, although they did not find any unstable growth regions. To the authors knowledge, there have been no real-gas receptivity studies for other types of freestream disturbances, namely entropy and vorticity disturbances.

The flow conditions and geometry for this study are the same as that of Knisely and Zhong,[2,3] which themselves are similar to the conditions used by Bitter and Shepherd.[26] This configuration features a moderate amount of real-gas and wall-cooling effects. The objective of the current study is to better understand the receptivity of a hypersonic boundary layer to a freestream entropy pulse with real-gas and nose bluntness effects. Future studies will include other types of disturbances to obtain a fuller picture of the receptivity process.

II. Simulation Conditions

As mentioned earlier, flow conditions for this study (summarized in Tables 1 and 2) are taken from Knisely and Zhong.[2,3] The geometry is an axisymmetric blunt cone with a half-angle of 5 degrees. Case 1 uses a nose radius of $r_N = 1$ mm and the same steady meanflow as the cold-wall case of Knisely and Zhong.[2,3] Case 2 uses a nose radius of $r_N = 25$ mm. The wall is isothermal at a translation-rotation temperature of 300 K. The flow at the wall is in thermal equilibrium such that $T_w = T_{v,w}$. For Case 2 the non-catalytic boundary condition was used. For Case 1, the super-catalytic boundary condition was used to improve convergence downstream. However, numerical tests in both unsteady DNS and LST revealed no significant differences in stability characteristics between a noncatalytic and super-catalytic wall, probably due to the low wall temperature.

The DNS grid uses 256 points in the wall-normal direction for Case 1. The DNS grid used 512 points in the wall-normal direction for Case 2 to account for the larger shock height. Four points are used in the azimuthal direction. The streamwise grid resolution in Case 1 varies from 86 points per millimeter near the nose to 10 grid points per millimeter downstream. The streamwise grid resolution for Case 2 varies from 14 grid points per millimeter near the nose to 5 grid points per millimeter downstream.

Table 1. Freestream conditions for DNS simulations.

Parameter	Value	Parameter	Value
M_∞	5	$H_{0,\infty}$	9.17 MJ/kg
ρ_∞	2.322-2$\times10^{-2}$ kg/m^3	p_∞	10 kPa
T_∞	1491.3 K	U_∞	3882.42 m/s
Re_1	1.7191$\times10^6$ m^{-1}	α	0 deg
c_{N_2}	0.78	c_{O_2}	0.22

Table 2. Wall conditions for DNS simulations.

Parameter	Value
T_w	300 K
$T_w/T_{0,\infty}$	3.9%

III. Governing Equations and Gas Model

The DNS and LST codes were originally developed by Mortensen and Zhong.[27–32] The governing equations are formulated for thermochemical nonequilibrium with a two-temperature model for the translation-rotation and vibrational energy modes. The rotational mode is assumed to be fully excited. As mentioned

earlier, the five-species model (N_2, O_2, NO, N, and O) is used to simulate air. The governing equations are the Navier-Stokes equations, here written in conservative form. The set of equations include 5 species mass conservation equations, 3 momentum conservation equations, the total energy equation, and the vibration energy equation. The governing equations in vector form are written as:

$$\frac{\partial U}{\partial t} + \frac{\partial F_j}{\partial x_j} + \frac{\partial G_j}{\partial x_j} = W \tag{1}$$

where U is the state vector of conserved quantities, W is the source terms, and F_j and G_j are the inviscid and viscous flux vectors respectively. Further details can be found in the work of Mortensen and Zhong.[27]

IV. Numerical Methods

A. DNS

The thermochemical nonequilibrium DNS code used here is a high-order shock-fitting finite difference code developed by Mortensen and Zhong.[27–32] The shock-fitting formulation is useful here because it avoids shock smearing and oscillations near shocks, allowing the usage of high-order schemes. After the flowfield and shock position is initialized, the shock position is advanced in time alongside the flowfield. To apply the finite difference method, the Navier-Stokes equations must be transformed into computational space as follows

$$\frac{1}{J}\frac{\partial U}{\partial \tau} + \frac{\partial E'}{\partial \xi} + \frac{\partial F'}{\partial \eta} + + \frac{\partial G'}{\partial \zeta} + \frac{\partial E'_v}{\partial \xi} + \frac{\partial F'_v}{\partial \eta} + + \frac{\partial G'_v}{\partial \zeta} + U\frac{\partial (1/J)}{\partial \tau} = \frac{W}{J} \tag{2}$$

where J is the Jacobian of the coordinate transformation. More details about this transformation can be found in the work of Mortensen.[32] The seven-point finite-difference stencil of Zhong[33] is used to discretize the spatial derivatives

$$\frac{\partial f_i}{\partial x} = \frac{1}{hb_i}\sum_{k=-3}^{3} \alpha_{i+k} f_{i+k} - \frac{\alpha}{6!b_i} h^5 \left(\frac{\partial f^6}{\partial^6 x}\right) \tag{3}$$

where h is the step size. Setting $\alpha < 0$ yields a fifth order upwind explicit scheme whereas $\alpha = 0$ reduces to a sixth order central scheme. The inviscid terms use $\alpha = -6$ which yields a low dissipation fifth order upwinded difference and the viscous terms are discretized using $\alpha = 0$. Derivatives in the azimuthal direction are computed through Fourier collocation. In order to compute second derivatives, the first order derivative operator is applied twice. Flux splitting is used for the inviscid flux terms with the eigenvalues of Λ for thermochemical nonequilibrium derived by Liu and Vinokur.[34]

Conditions behind the shock are calculated from the Rankine-Hugoniot relations. The freestream is assumed to be frozen and in thermal equilibrium and the shock is assumed to be infinitely thin so that chemical compositions and the vibration temperature do not change across the shock. Further details on the thermochemical nonequilibrium shock fitting method can be found in Prakash *et al.*[35] In this study the forward Euler method is used to advance the solution in time.

B. LST

The LST code used here is that of Knisely and Zhong,[36] which expands on the original code of Mortensen.[32] The code partially relaxes the parallel meanflow assumption, and the meanflow wall-normal velocity is no longer assumed to be zero. In addition, freestream shock boundary conditions developed by Knisely and Zhong[36] have been implemented. The LST equations are derived from the Navier-Stokes equations by a perturbation expansion of the form $q = \overline{q} + q'$, where q represents the value of any flow quantity, $\overline{q}$ is the meanflow quantity, and q' is the perturbation quantity. The steady flow terms can then be removed under the assumption that they satisfy the governing equations themselves. The perturbation quantities are assumed to be small such that higher order terms can be ignored and the meanflow terms are assumed to be function of y only. The perturbation terms are then assumed to take the form of a normal mode such that $q' = \hat{q}(y)\exp\left[i\left(\alpha x + \beta z - \omega t\right)\right]$, where ω is the circular frequency of the disturbance and α and β are the wavenumbers. This study is concerned with spatial stability, such that ω is real and specified a priori. In addition, α will be assumed to be complex such that $\alpha = \alpha_r + i\alpha_i$. In spatial stability theory, α_r is the streamwise wavenumber and $-\alpha_i$ is the growth rate. A positive value for $-\alpha_i$ corresponds to

growth whereas a negative value of $-\alpha_i$ corresponds to decay. Substituting the normal mode form of the perturbation quantity into the governing equations then yields a set of $ns+5$ coupled ordinary differential equations of the form

$$\left(\mathbf{A}\frac{d^2}{dy^2}+\mathbf{B}\frac{d}{dy}+\mathbf{C}\right)\vec{\phi}=\vec{0}. \tag{4}$$

where $\vec{\phi}=\left[\hat{\rho}_1,\hat{\rho}_2,\ldots,\hat{\rho}_{ns},\hat{u},\hat{v},\hat{w},\hat{T},\hat{T}_V\right]^T$, $\mathbf{A}$, $\mathbf{B}$ and $\mathbf{C}$ are complex square matrices of size $ns+5$, and ns is the number of species in the gas model. This is now a boundary value problem suitable for numerical discretization.

Eq.4 can be transformed into computational space so that numerical derivatives can be calculated. The first and second derivative operators in the wall-normal direction are discretized using Lagrange polynomials with a five-point stencil, which results in a 4th-order accurate method. The wall boundary conditions are linearized non-catalytic conditions for density, no slip, zero temperature perturbation and pressure extrapolation. In the freestream, the shock boundary conditions developed by Knisely and Zhong[36] were used.

Although LST cannot predict amplitudes, it can still be used to estimate boundary-layer transition locations by using the semi-empirical e^N method, with e^N is defined as

$$e^N=\frac{A(s)}{A_0}=\exp\left[\int_{s_0}^{s}-\alpha_i(s,f)ds\right] \tag{5}$$

where $A(s)$ is the disturbance amplitude at a streamwise location s downstream of the branch I neutral point, A_0 is the initial disturbance amplitude, s_0 is the location where the disturbance first becomes unstable (referred to as the branch I neutral stability point) and N is the N-factor. The integration is performed using the trapezoidal method. In-flight transition N-factors are typically between 5 and 10, whereas ground test N-factors can be considerably lower. As will be explained later, N-factors can be used to isolate the receptivity coefficients of the second mode from the overall disturbance in a receptivity simulation.

C. Freestream Disturbance Model

The freestream pulse disturbances are simulated in unsteady DNS by superimposing the disturbance onto the steady freestream base flow. In this study the methodology of He and Zhong[11] is used and the freestream disturbance is modeled as a planar Gaussian pulse, allowing a broad range of frequencies to be excited simultaneously. The freestream is assumed to be frozen and in thermal equilibrium. The local disturbance at a point (x,y,z) at time t associated with a weak planar Gaussian pulse at zero incidence-angle is

$$\begin{bmatrix}u'\\v'\\P'\\\rho'\end{bmatrix}_\infty=\begin{bmatrix}\Delta u\\\Delta v\\\Delta P\\\Delta\rho\end{bmatrix}_\infty\exp\left(-\frac{R_c^2}{2\sigma^2}\right) \tag{6}$$

where Δ denotes the amplitude of the disturbance, R_c is the horizontal distance to the center of the pulse and σ is a nondimensional quantity which determines both the shape and frequency content of the pulse. For a planar pulse,

$$R_c=\sqrt{(x-x_c)^2} \tag{7}$$

$$x_c=x_0+u_pt \tag{8}$$

where x_c is the location of the center of the pulse at time t, x_0 is the initial location of center of the pulse, and u_p is the pulse velocity. Entropy waves convect with the fluid such that $u_p=\overline{u}_\infty$. In a shock-fitting formulation, the freestream is outside of the computational domain and cannot be simulated directly. The effect of freestream disturbances on the flow-field is instead modeled through the shock boundary conditions. The conditions at the points located immediately behind the shock are determined by applying the Rankine-Hugoniot relations with the unsteady freestream quantities specified through the disturbance model.

For simplicity, the entropy wave model of Ma and Zhong[6] will be used here, where the disturbance is specified in density-pressure form rather than entropy-pressure form. The dispersion relation for an entropy wave can be written as follows:

$$\frac{\Delta\rho}{\overline{\rho}_\infty} = -\epsilon M_\infty \tag{9}$$

$$\frac{\Delta P}{\overline{P}_\infty} = \frac{\Delta u}{\overline{U}_\infty} = \frac{\Delta v}{\overline{U}_\infty} = 0 \tag{10}$$

where ϵ is a small nondimensional parameter representing the wave magnitude. The sign convention is chosen so that a positive value of ϵ corresponds to an increase in temperature and entropy, thereby representing a "hotspot" disturbance. In general, the corresponding disturbance in entropy can be computed as $\Delta s/c_p = \ln(1+\epsilon)$. For a weak disturbance (like that used in this study), $\Delta s/c_p \approx \epsilon$ and the entropy can also be directly specified in the place of density like in the theoretical model of McKenzie and Westphal.[4]

The other variables required for input into the thermochemical nonequilibrium shock-fitting model can be computed from the assumptions of the freestream gas model. Using the perfect gas equation of state, the temperature perturbation is the negative of the density perturbation. Under the assumption of thermal equilibrium, the vibration-temperature perturbation is set equal to the translation-rotation temperature perturbation. Finally, under the assumption of non-reacting flow, the species density perturbation can be calculated as the product of the overall density perturbation and the fixed species mass fraction c_s.

$$\frac{\Delta T}{\overline{T}_\infty} = \frac{\Delta T_v}{\overline{T}_\infty} = \epsilon M_\infty \tag{11}$$

$$\frac{\Delta \rho_s}{\overline{\rho}_\infty} = -\epsilon c_s M_\infty \tag{12}$$

The pulse parameters for this study are given in Table 3 was superimposed on to the steady base flow. The pulse shape and amplitude spectrum in the freestream are shown in Figure 1. The parameter σ was chosen so that all unstable frequencies in Case 1 were resolved. From the stability map in Figure 14, the highest unstable frequency is around $f = 1600$ kHz. The amplitude spectrum indicates that the amplitude at $f = 2000$ kHz is only about 3 times smaller than the peak amplitude. Therefore the selected parameter value should be adequate to resolve the relevant second-mode frequencies. The unstable frequencies are expected to be smaller for Case 2 due to the nose bluntness effect, so the selected value σ should be adequate for Case 2 as well. In addition, the pulse radius for the selected value of σ is around 1.5 mm. The pulse magnitude ϵ used in this study is chosen to ensure a linear disturbance downstream while ensuring that the convergence error does not contaminate the solution.

Table 3. Pulse parameters for receptivity simulation.

Parameter	Case 1	Case 2
ϵ	2E-6	2E-6
σ	5E-4	5E-4
x_0	-0.04 m	-0.015 m

D. FFT

Once the entropy pulse has entered the shock layer and the resulting disturbance has passed through the domain for one zone, temporal FFT is applied to the time-history of each variable. The disturbance quantity for a single frequency can then be written as follows:

$$\phi'(x,y,t) = |\Delta\phi(x,y)| \exp\left[i\left(\psi(x,y) - 2\pi f t\right)\right] \tag{13}$$

where ϕ' represents the disturbance of some variable, $|\Delta\phi|$ is the amplitude for a single frequency and ψ is the phase angle at that frequency. The local growth rate, streamwise wave number and phase speed (typically nondimensionalized by the freestream velocity) of each frequency can then be calculated by:

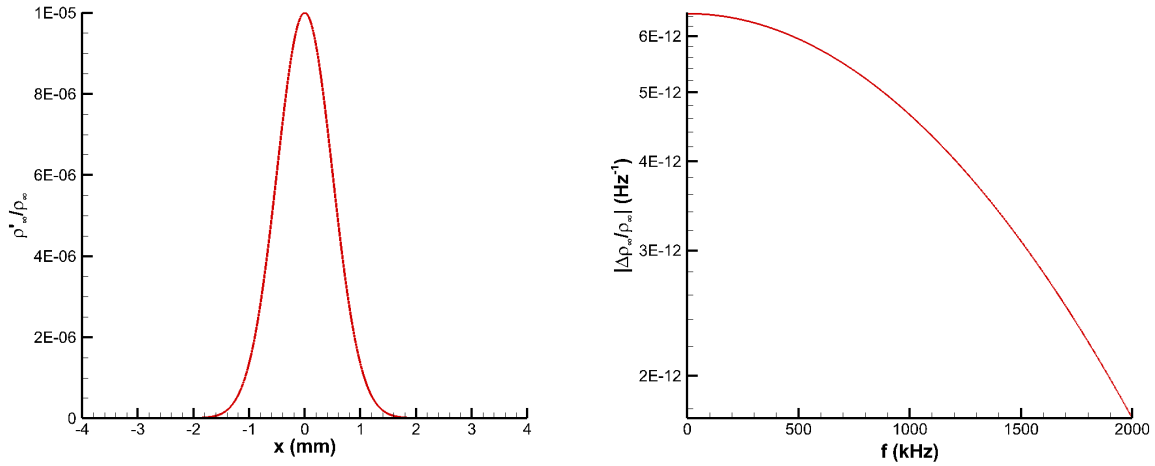

(a) (b)

Figure 1. Freestream pulse (a) shape and (b) amplitude spectrum

$$-\alpha_i(f) = \frac{1}{|\Delta\phi(f)|}\frac{d|\Delta\phi(f)|}{ds} \tag{14}$$

$$\alpha_r(f) = \frac{d\psi(f)}{ds} \tag{15}$$

$$c_r(f) = \frac{2\pi f}{\alpha_r(f)} \tag{16}$$

To identify the frequencies that undergo the largest amplification, the pressure amplitude spectrum at each streamwise distance must be normalized by the amplitude spectrum of the freestream pulse. This yields an amplitude ratio transfer function which can be used to determine the wall pressure disturbance amplitude at any streamwise distance. Since there is no freestream pressure disturbance for an entropy wave, both the wall pressure disturbance and freestream density disturbance must be normalized by their corresponding freestream steady values. Following the work of Huang,[37] the normalized amplitude is computed using the following expression:

$$\text{Normalized amplitude} = \frac{|\Delta P(f)/P_\infty|}{|\Delta\rho_\infty(f)/\rho_\infty|} \tag{17}$$

V. Steady DNS Results

A. Case 1 Steady DNS Results

The steady flow-field solution in the nose region for Case 1 is presented below. The translation-rotation temperature, vibrational temperature, and some mass fraction contours for the nose region of the cone are shown in Figures 2 and 3. The highest temperatures, both translation-rotation and vibration, are encountered near the stagnation region. There is also strong thermal nonequilibrium in the nose region, with vibration temperatures that are noticeably smaller than translation-rotation temperatures. Moving downstream, thermal nonequilibrium effects decay and the translation-rotation and vibration temperatures begin to approach one another. Figure 3 indicates the presence of chemical nonequilibrium as well. O_2 dissociation is the most prominent reaction in the flow-field, with mass fraction values ranging from 0.14 to 0.22. The dissociation of O_2 into O can also be seen clearly in the mass fractions of O. Chemical

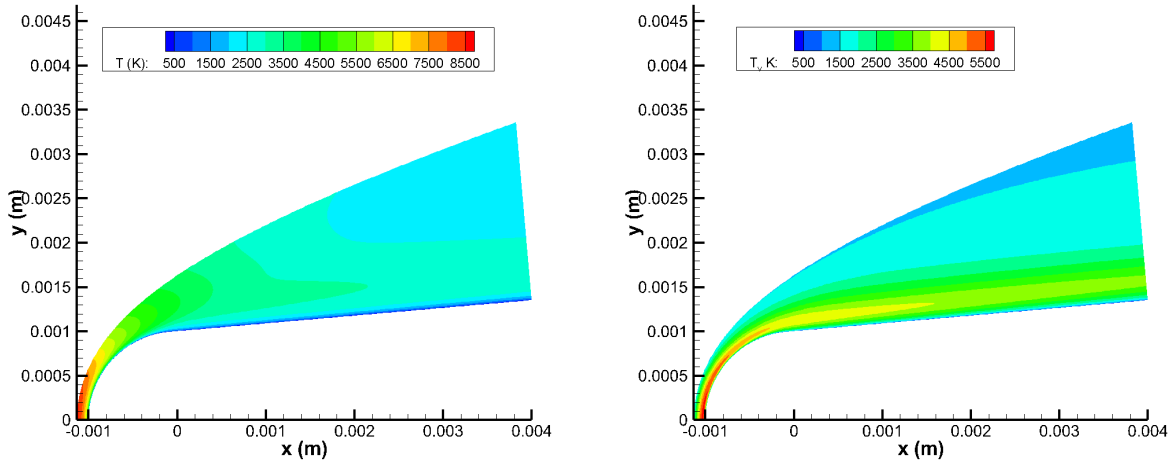

(a) (b)

Figure 2. Steady DNS contours in nose region for Case 1. (a) T and (b) T_v.

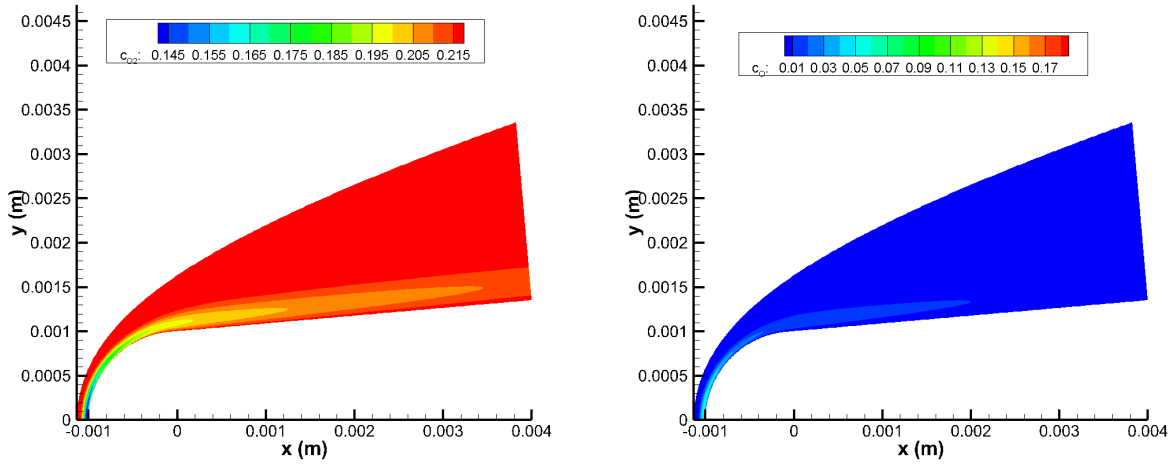

(a) (b)

Figure 3. Steady DNS contours in nose region for Case 1. Mass fractions of (a) O_2 and (b) O

nonequilibrium effects are strongest near the stagnation point due to the high temperatures there and decay downstream.

Figure 4 presents the streamwise variation of the near-wall total enthalpy profiles for Case 1 at various streamwise distances. The ordinate is the wall-normal distance. Comparing Fig. 4a to Fig. 4b, its apparent that the entropy layer is well within the boundary layer even at $s = 0.050$ m. This is characteristic of the flowfield over sharp nose geometries; the entropy layer is swallowed by the boundary layer very early in the flowfield. Here, the minimum entropy is always located at the wall because the wall temperature is much lower than the edge temperature. Moving downstream, this peak shifts upwards alongside the boundary layer. Eventually, the entropy peak converges onto a constant value.

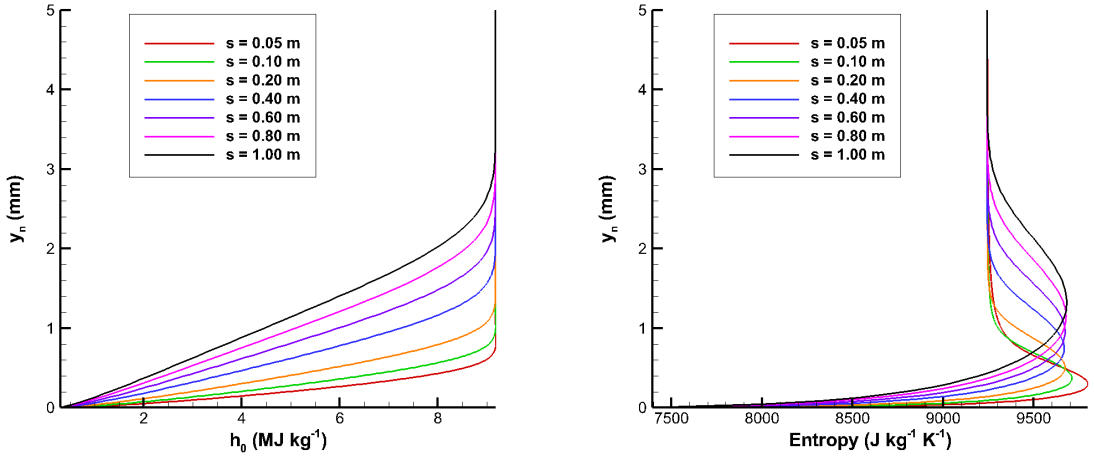

(a) (b)

Figure 4. Case 1 near-wall (a) total enthalpy and (b) entropy profiles at various distances

Figure 5 shows the streamwise variation in near-wall temperature profiles for Case 1. Initially, the peak in translation-rotation temperature is very high but weakens moving downstream. Like the entropy profile, the peak remains constant in strength after about $s = 0.4$ m. Initially the vibration temperature is much lower than the translation-rotation temperature. As a consequence, there is energy transfer from the translation-rotation modes to the vibration mode. Moving downstream, the temperature ratio starts to approach the edge values. That is, the vibration temperature and the translation-rotation temperature converge toward one another, and the flow starts to reach thermal equilibrium.

Figures 6 and 7 show the streamwise variation of the near-wall mass fraction profiles of all five species in the gas model. The minimum mass fraction of N_2 and O_2 and the peak mass fraction of the other species correspond to the location of strongest chemical nonequilibrium effects. This peak is strongest upstream and decreases in amplitude moving downstream. The location of these peaks roughly corresponds with the location of peak translation-rotation and vibration temperature. Quantitatively speaking, however, mass fractions do not vary much from their freestream mass fractions.

B. Case 2 Steady DNS Results

The steady flow-field solution in the nose region for Case 2 is presented in Figures 8 and 9. Interestingly, the contours indicate that the maximum translation-rotation temperature has not increased much compared to Case 1. The same trend is seen with the vibration temperature. However, it appears that the region of variation in vibrational temperature is much larger than in Case 1. Figure 9 indicates that chemical nonequilibrium effects are much stronger than in Case 1. O_2 mass fractions reach much smaller values in the stagnation region and towards the downstream region, indicating the presence of stronger O_2 dissociation. Likewise, O mass fractions reach much larger values. Near the stagnation point, the region of O_2 dissociation is larger relative to the shock height. Unlike Case 1, the region of O_2 dissociation remains attached to the wall due to the noncatalytic boundary condition. Its clear that chemical nonequilibrium effects persist further downstream compared to Case 1.

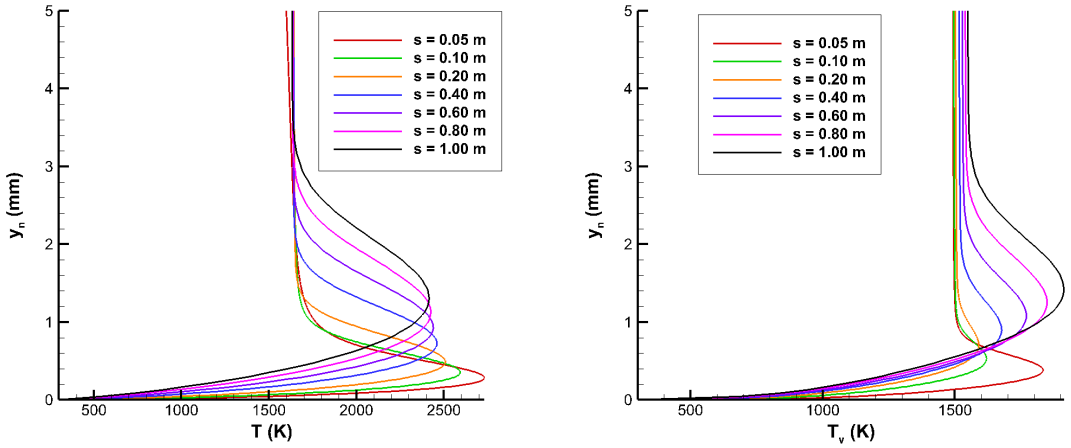

(a) (b)

Figure 5. Case 1 near-wall (a) translation-rotation temperature and (b) vibration temperature profiles at various streamwise distances

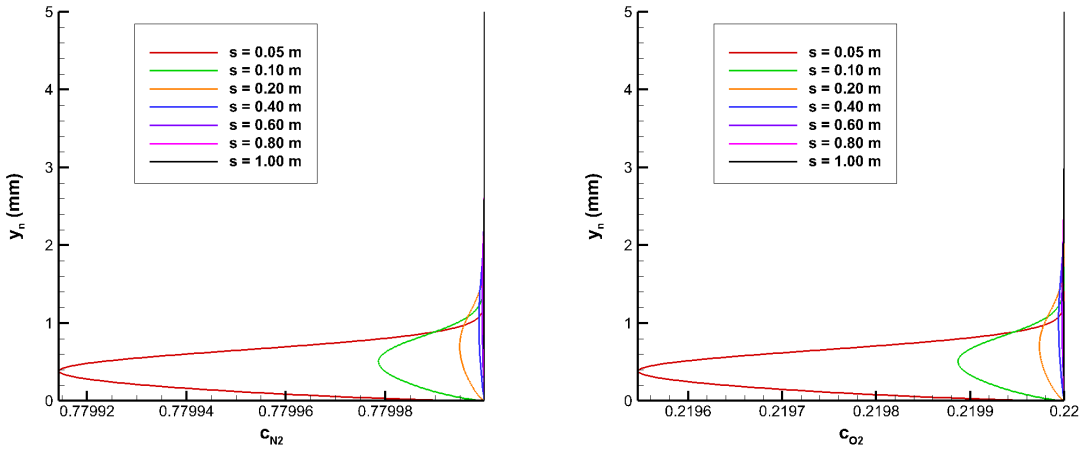

(a) (b)

Figure 6. Case 1 mass fraction profiles of (a) N_2 and (b) O_2 at various streamwise distances

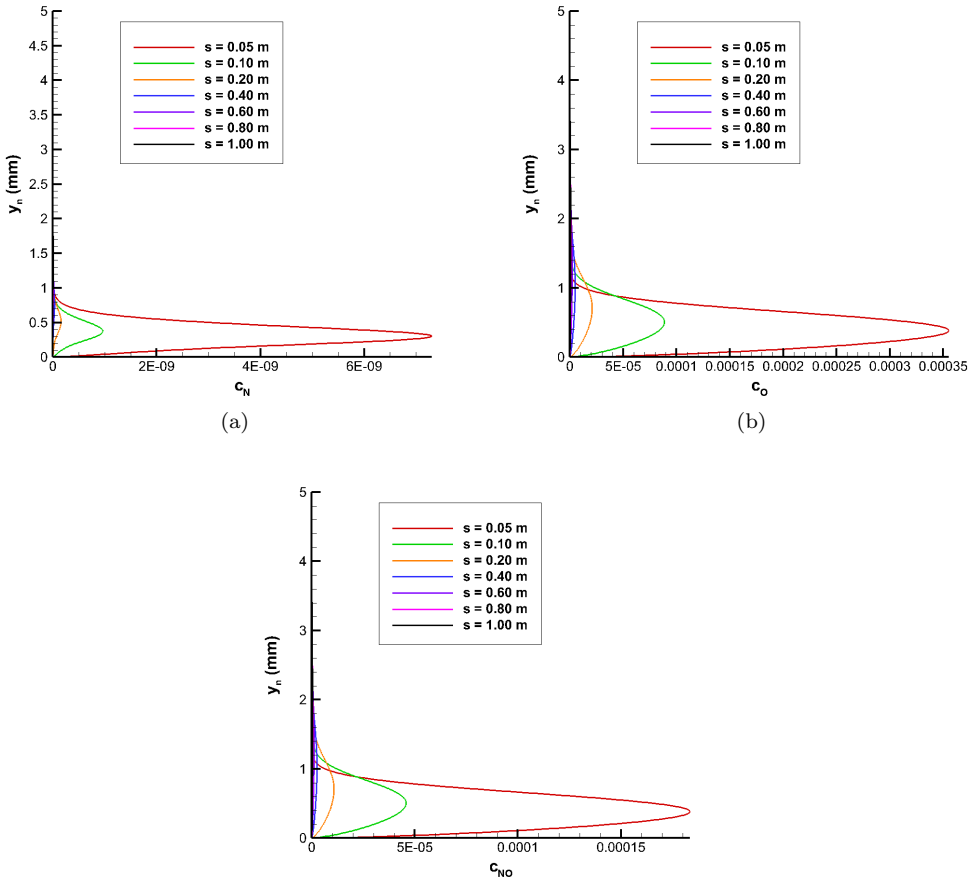

(a) (b) (c)

Figure 7. Case 1 mass fraction profiles of (a) N, (b) O, and (c) NO at various streamwise distances

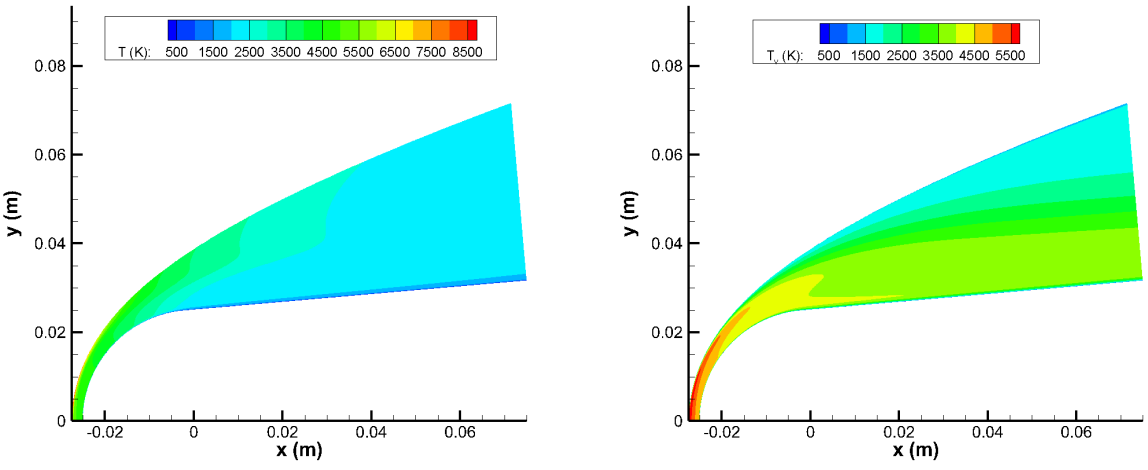

(a) (b)

Figure 8. Steady DNS contours in nose region for Case 2. (a) T and (b) T_v.

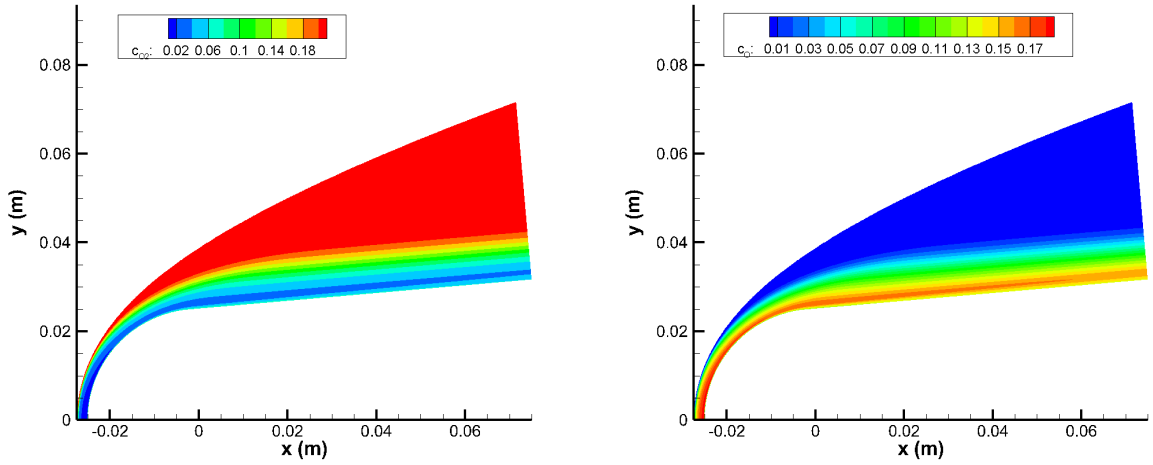

(a) (b)

Figure 9. Steady DNS contours in nose region for Case 2. Mass fractions of (a) O_2 and (b) O

Figure 10 presents the near-wall total enthalpy and entropy profiles for Case 2 at various streamwise locations. The entropy layer tends to reduce local velocities and thus local Reynolds number as well. Accordingly, the boundary layer thickness is large compared to Case 1. Here, there is also a small peak in the profile. This peak becomes larger and shifts towards the wall moving downstream. Figure 10b presents the entropy profile at the same streamwise locations. One of the most notable effects of nose bluntness is the delay of entropy layer swallowing. For a blunt nose, the entropy layer becomes considerably larger and the entropy layer swallowing distance will occur much later on the cone. In Case 2, it is clear that the entropy layer is much thicker than the boundary layer even at $s = 1.0$ m. Consequently, the entropy layer swallowing distance will be located even further downstream. The maximum entropy is larger than Case 1 due to higher vibration temperatures seen in Figure 11.

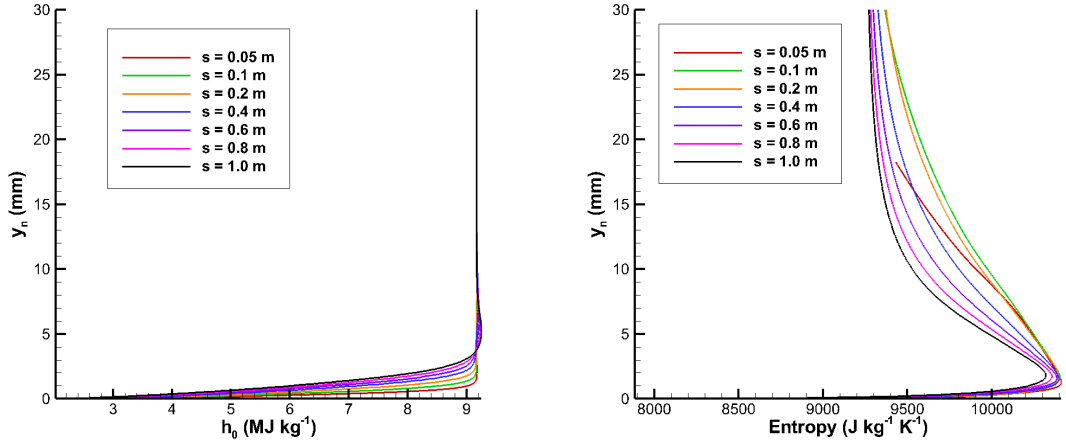

(a) (b)

Figure 10. Case 2 (a) total enthalpy and (b) entropy profiles at various streamwise distances

Figure 11 presents the near-wall temperature profiles for Case 2 at various streamwise locations. Initially, the maximum in translation-rotation temperature is located at the shock itself. Moving downstream, the

profile takes a different shape. A local peak in temperature is formed, which then shifts towards the wall moving downstream. Beyond $s = 0.1$ m, a smaller secondary peak is generated close to the wall. This secondary peak becomes larger whereas the the primary peak remains relatively constant moving downstream. Note that the translation-rotation temperature is only slightly larger than in Case 1. On the other hand, the overall vibration temperature is much larger than in Case 1 at all streamwise locations. In fact, the vibration temperature is larger than translation-rotation temperature. This result reinforces the necessity of including thermal nonequilibrium effects especially to accurately predict blunt nose flow-fields. While the translation-rotation temperature remains largely constant downstream, the peak vibration temperature rapidly decreases.

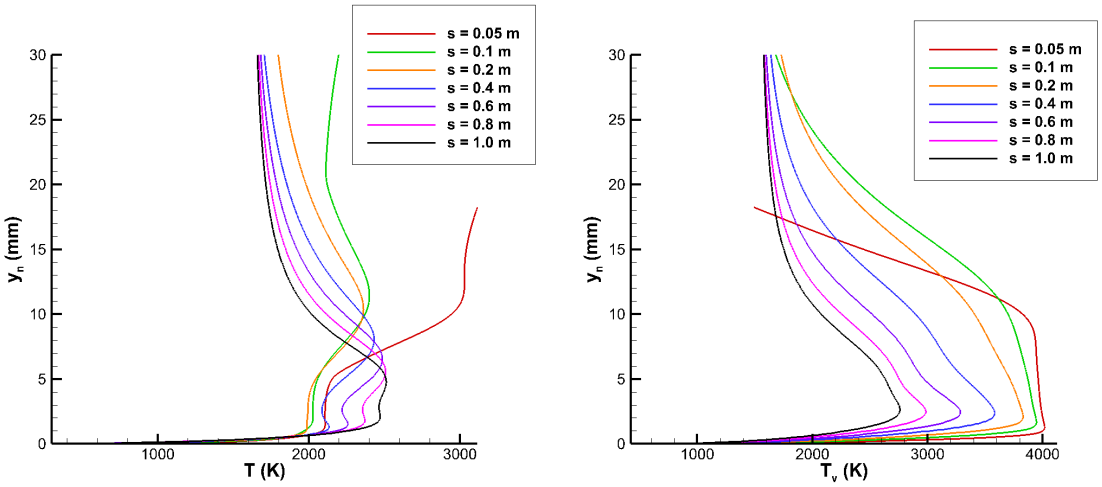

(a) (b)

Figure 11. Case 2 (a) Translation-rotation temperature and (b) vibration temperature vs. wall-normal distance at various streamwise distances

Figures 12 and 13 present the near-wall mass fraction profiles for Case 2. Looking at the profiles for N_2 and O_2, its clear that chemical nonequilibrium effects are much stronger than Case 1. N_2 mass fractions vary between 0.78 to 0.75, whereas O_2 mass fractions vary between 0.22 and 0.03. Consequently, the mass fractions of O and NO are much higher than for Case 1. Since translation-rotation temperatures are comparable to Case 1, this increase in chemical nonequilibrium is due to the large increase in vibration temperature. These profiles are similar to the results of Mortensen,[22] who found that the overall mass fraction of O increases substantially with increasing nose bluntness. As mentioned earlier, Mortensen showed that this increase in O actually destabilizes the supersonic mode due to the fact that recombination of O into O_2 is exothermic.

,

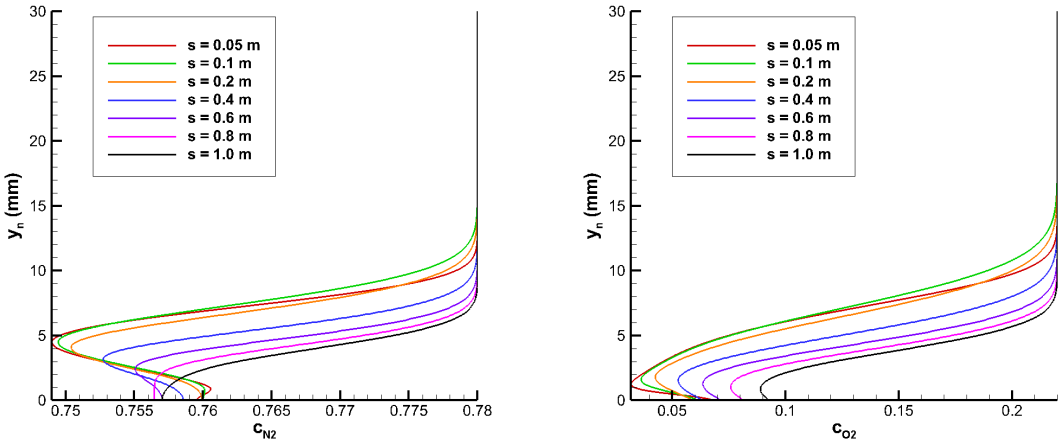

(a) (b)

Figure 12. Case 2 mass fractions profiles of (a) N_2 and (b) O_2 at various streamwise distances

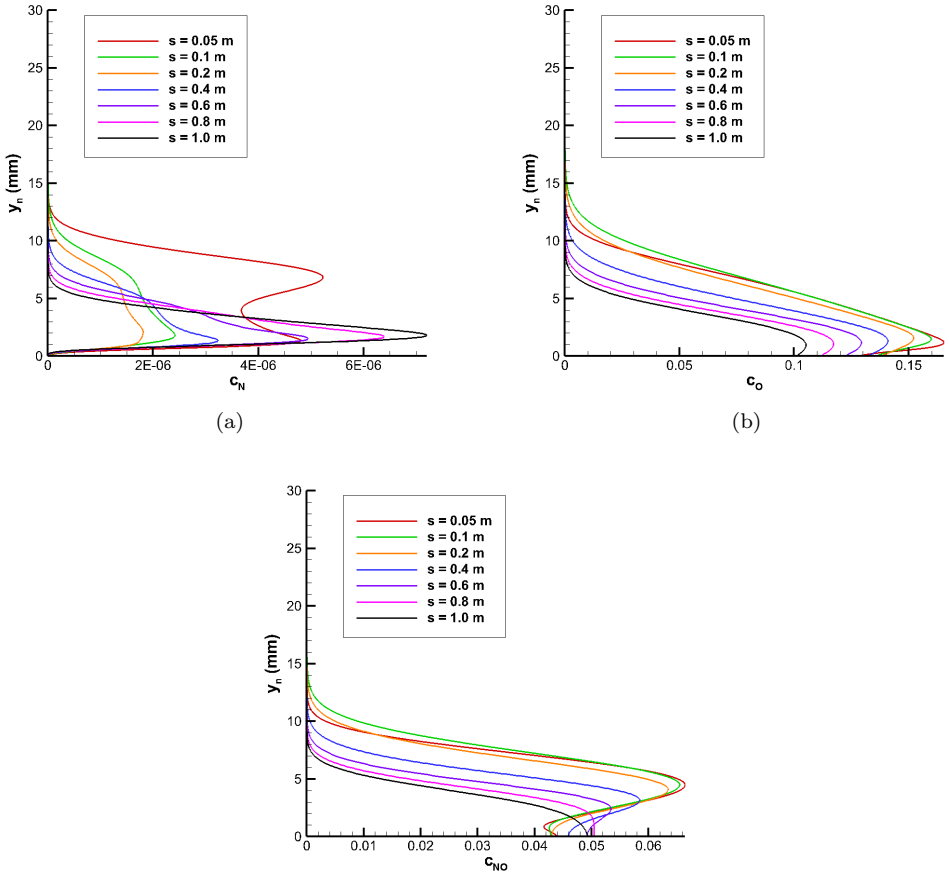

(a) (b)

(c)

Figure 13. Case 2 mass fraction of (a) N, (b) O, and (c) NO at various streamwise distances

VI. LST Results

A. Case 1 LST Results

After converging the steady meanflow, Linear Stability Theory (LST) calculations were performed for Case 1. The second mode was identified as the fast acoustic mode, mode F1. A streamwise marching procedure was performed for a number of frequencies of mode F1, generating the stability map in Fig. 14. Points inside of this line correspond to a positive growth rate, and points outside of the line correspond to a negative growth rate. The second mode first becomes unstable around $s = 0.1$ m at $f = 1500$ kHz. The unstable frequencies can be very high because the boundary layer is extremely thin, due to the low wall temperature. Below $f = 740$ kHz, mode F1 synchronizes with the slow acoustic spectrum before becoming stable again. This generates an unstable supersonic mode which can be identified by the broadening of the branch II neutral stability curve. Above $f = 740$ kHz, mode F1 becomes stable again before synchronization with the slow acoustic spectrum. It should be noted that upon synchronization with the slow acoustic spectrum, the unstable mode F1 actually bifurcates into two distinct modes.[26] With this bifurcation in mind, the unstable fast acoustic mode will be referred to as mode $F1^{+}$ and the newly created mode will be referred to as mode $F1^{-1}$ when the distinction is necessary.

The modal behavior can be seen more clearly in the streamwise growth rate and phase speed plots of Figure 15, presented for a frequency of $f = 600$ kHz. Mode $F1^{+}$ begins at a nondimensional phase speed near $c_r = 1 + 1/M_\infty$. The phase speed then decreases with streamwise distance. Eventually mode $F1^{+}$ synchronizes with mode S and mode $F1^{+}$ becomes unstable. After mode $F1^{+}$ reaches its maximum growth rate, it synchronizes with the slow acoustic spectrum and bifurcates into two distinct modes. At this point, mode $F1^{+}$ becomes a continuous mode and remains unstable, whereas mode $F1^{-}$ is discrete and is stable. At the slow acoustic synchronization point in Figure 15b, a "kink" is seen after the peak, at which mode $F1^{+}$ becomes supersonic and the growth region is extended. After mode $F1^{+}$ becomes stable, it coalesces with the slow acoustic spectrum and can no longer be resolved in the LST code. The LST code will then latch onto mode $F1^{-}$, which has a similar phase speed but different growth rates, creating the abrupt changes in growth rate past the branch II location on the stability map.

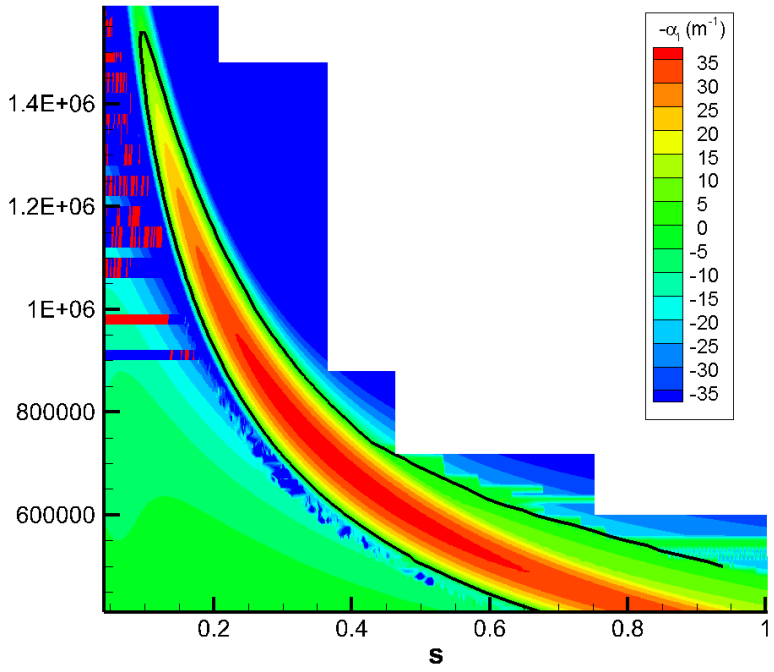

Figure 14. Case 1 neutral stability map for second mode. Black line indicates points of neutral stability.

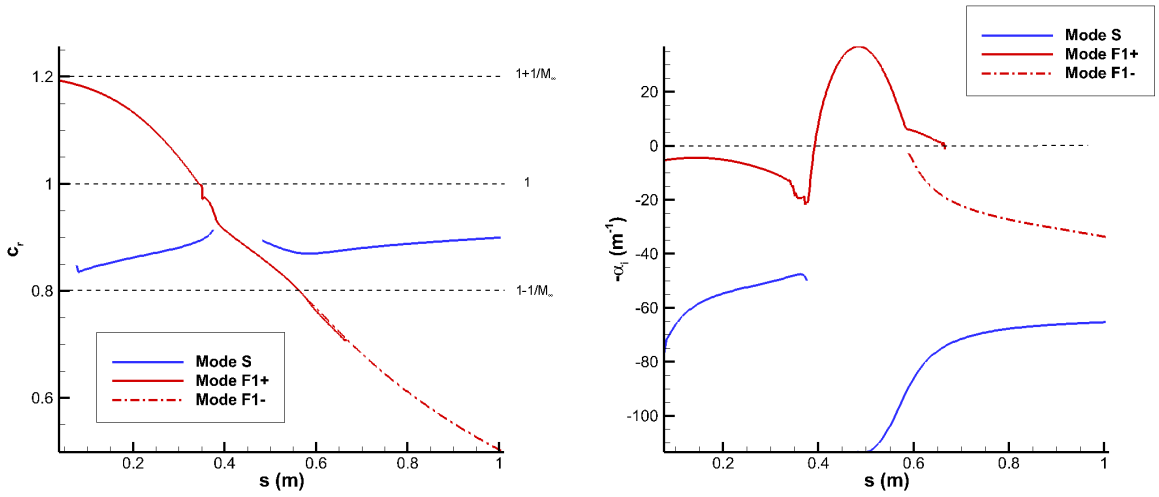

Figure 15. Case 1 (a) phase speed and (b) growth rate vs. streamwise distance for $f = 600$ kHz

N-factor curves for the second mode (mode F1/F1$^+$) are plotted in Figure 16. Lowering the frequency, the location of maximum N-factor shifts downstream and the maximum N-factor attained increases. Because of the unstable supersonic mode region below $f = 740$ kHz, the shape of the N-factor curves below this frequency flatten before reaching the peak, which is delayed further downstream. However, as noted by Knisely and Zhong,[2] the supersonic mode has little effect on the N-factor envelop (shown as the red line) because the maximum N-factor was pushed further downstream. The largest N-factor attained here is around $N = 8$ for a frequency of $f = 450$ kHz.

B. Case 2 LST Results

LST results have not yet identified a discrete mode in Case 2. Steady meanflows may need to be extended further downstream before a discrete mode can be definitively identified. Presumably, the second mode region for this case is much further downstream due to the delay of instabilities by the nose bluntness effect.

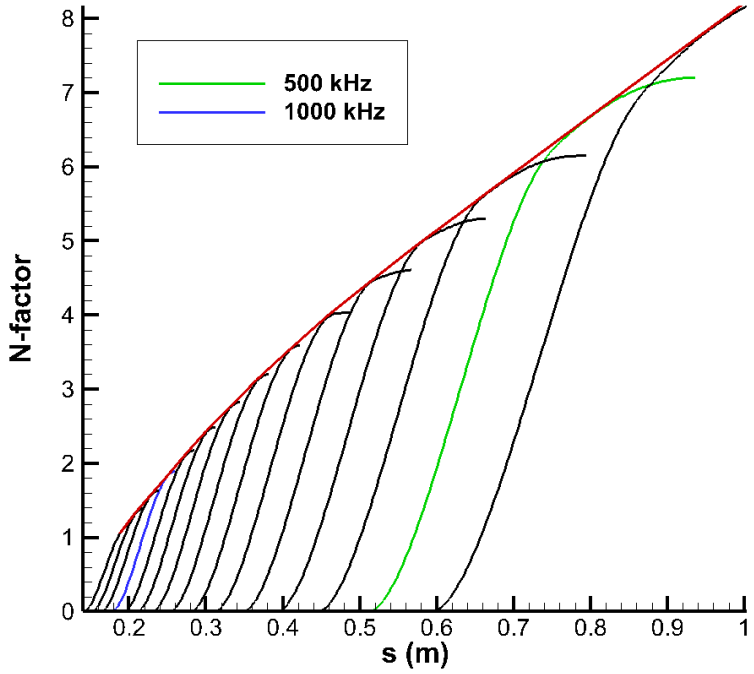

Figure 16. Case 1 N-factor curves for the second mode (mode F1$^+$). Frequency increments are Δf = 50 kHz. Red line is the N-factor envelop.

VII. Unsteady DNS Results

The freestream entropy pulse with the parameters specified in Table 3 was imposed onto the freestream. The disturbance that was then generated behind the shock was tracked as it propagated downstream. Fast Fourier Transform (FFT) was used to decompose the unsteady wall-pressure to obtain amplitudes, growth rates and phase speeds at each streamwise location. In Case 1, these results were then validated with LST and used to calculate receptivity coefficients.

A. Case 1 Unsteady DNS Results

The time trace of the wall-pressure disturbance at various upstream locations in Case 1 is presented in Figure 17. Starting from $s = 0.044$ m and moving downstream to $s = 0.104$ m, the wave packet has weakened due to the absence of significant boundary-layer instabilities. At this point, the wave packet is a jagged series of oscillations, likely due to a combination of a shock-disturbance front, forcing waves generated by the shock-disturbance interaction upstream, and a weak first mode. This shock-disturbance front occurs because the planar pulse is infinite in the y and z directions and thus continues to interact with the shock even as the disturbance within the shock layer propagates downstream. The shock-disturbance front can be clearly seen in the pressure and temperature contours of Figure 18. At $s = 0.175$ m, the rear of the wave packet has increased in amplitude slightly due to the second mode. By this point, frequencies higher than $f =$ 1200 kHz are well within the second mode unstable region. Moving downstream, the strength of the shock-disturbance front remains relatively constant while the rear of the wavepacket, associated with the second mode, undergoes strong amplification. At this point, the second-mode oscillations are around the same magnitude as those associated with the shock-disturbance interaction. By $s = 0.276$ m, the second-mode oscillations have begun to dominate the wave packet. The disturbance further downstream is shown in Figure 19. Here the second-mode oscillations have grown by an order of magnitude compared to those at $s = 0.276$ m and the shock-disturbance front is no longer visible. In fact, the amplitude of the shock-disturbance front is about 50 times smaller than the amplitude of the second mode here. This shape (though not necessarily

the amplitude) is retained by the wave packet through the end of the domain at $s = 1.0$ m.

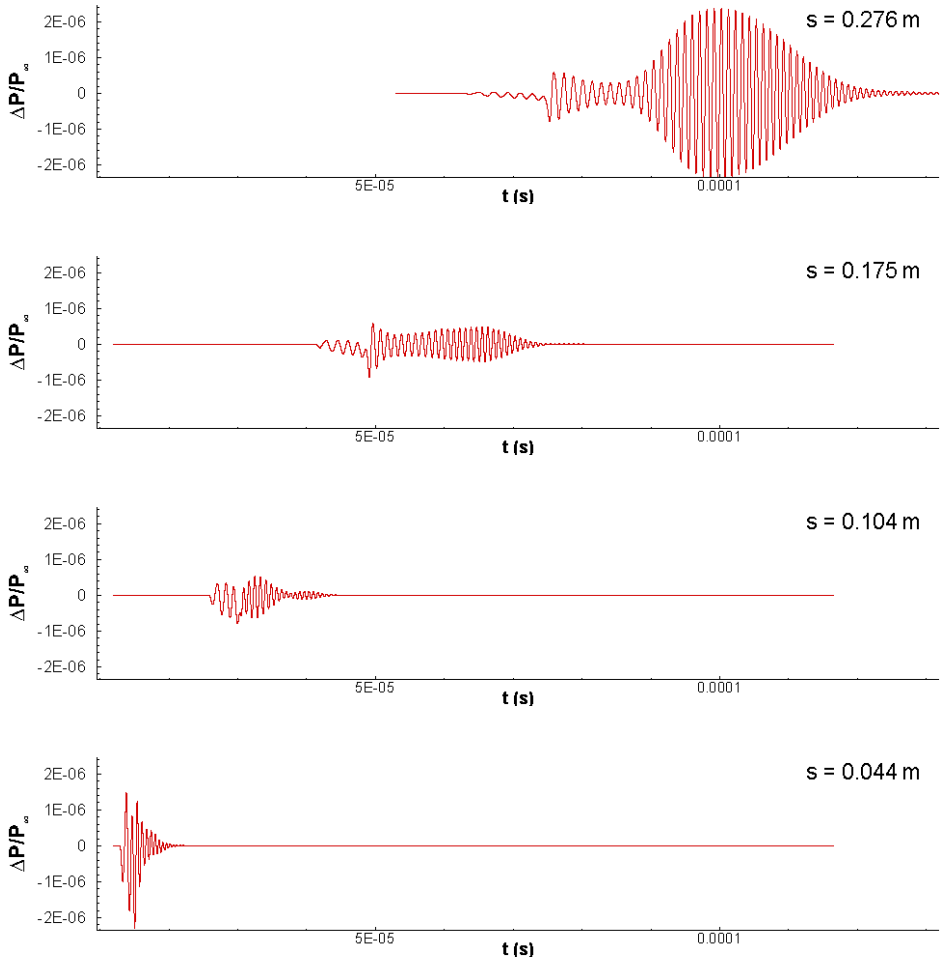

Figure 17. Case 1: Time trace of wall-pressure disturbance at various upstream streamwise distances

A more complete picture of the wavepacket can be seen through a full contour plot of the disturbance. Figure 20 presents a snapshot of the disturbance around $s = 0.5$ m. Note that the disturbance is propagating from the left to the right. The disturbance can be separated into two distinct regions. The front of the wave packet is the second mode. The rear of the wave packet, marked by a distinct change in the shape of the perturbation, is the supersonic mode. In fact, the acoustic-like waves emanating outside of the boundary layer are indicative of the supersonic mode. The supersonic mode trails behind the second mode because it travels at a phase speed $c_r < 1-1/M_\infty$ whereas the second mode travels at a phase speed $1-1/M_\infty < c_r < 1+1/M_\infty$.

As mentioned earlier, the unsteady wall-pressure at each streamwise location was decomposed using FFT. The resulting amplitude spectrum was then normalized by the amplitude spectrum of the freestream disturbance to account for the non-uniformity of the initial disturbance spectrum. The contour of normalized amplitudes for the entire domain is shown in Figure 21. It is clear that the planar entropy pulse has excited significant second-mode instabilities, as evidenced by the large amplitudes downstream. The most amplified frequency appears to be around $f = 470$ kHz. This agrees well with the N-factor contours derived from LST. Recall that the branch II neutral stability curve is the point at which disturbances become stable again. This point then corresponds to the location at which a particular frequency reaches its peak amplitude. Comparing the DNS to LST, the location of peak amplitude agrees well with the branch II neutral stability curve.

The normalized wall-pressure amplitude further upstream is presented in Figure 22. Here the contours are re-scaled to better highlight disturbance excitation due to forcing waves from the shock-disturbance interaction upstream. The black line indicates the LST-derived neutral stability curves. Below $f = 300$ kHz,

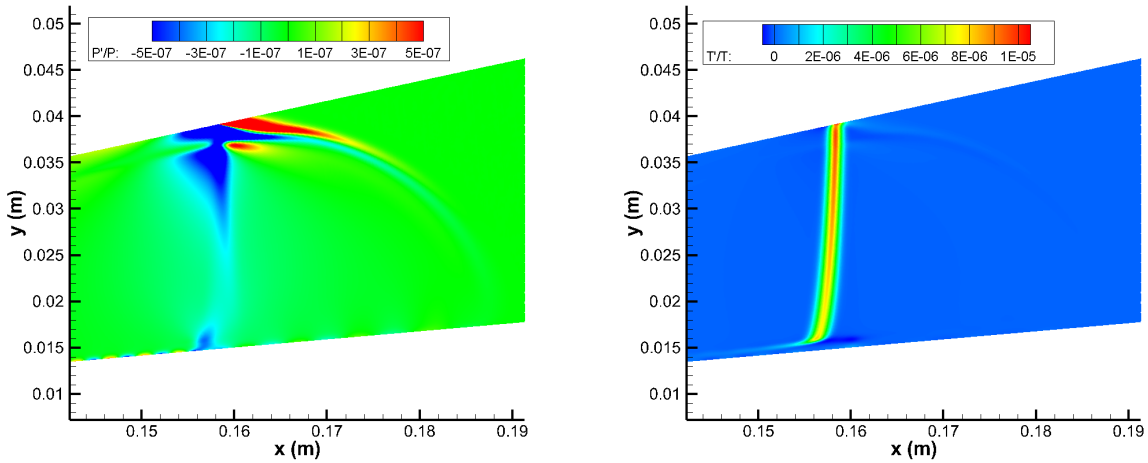

(a) (b)

Figure 18. Case 1 (a) pressure and (b) translation-rotation temperature contours displaying the shock-disturbance front

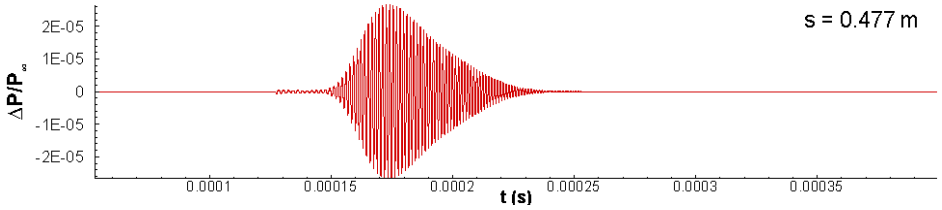

Figure 19. Case 1: Time trace of wall-pressure disturbance at a downstream location

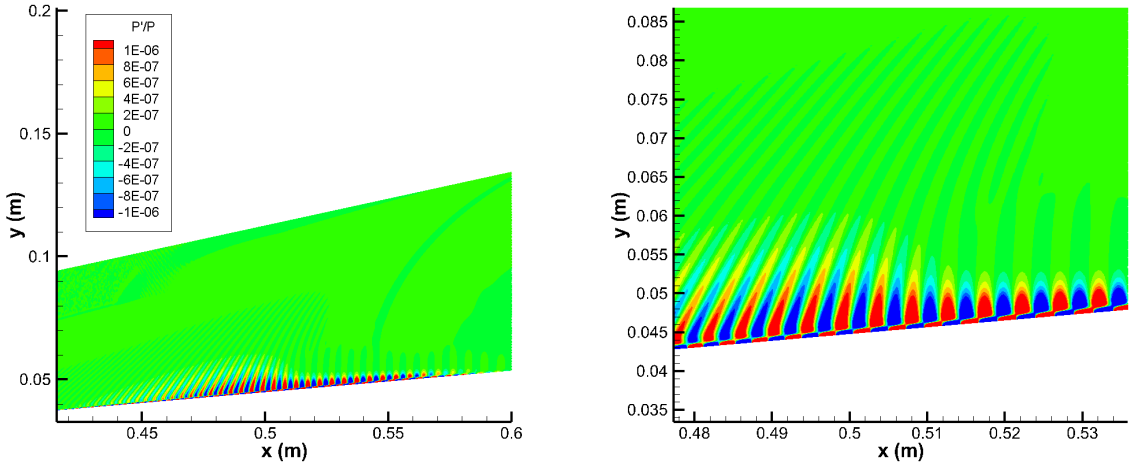

(a) (b)

Figure 20. Case 1 unsteady pressure perturbation contours near x = 0.5 m. Note the waves radiating outside the boundary layer, indicating the supersonic mode.

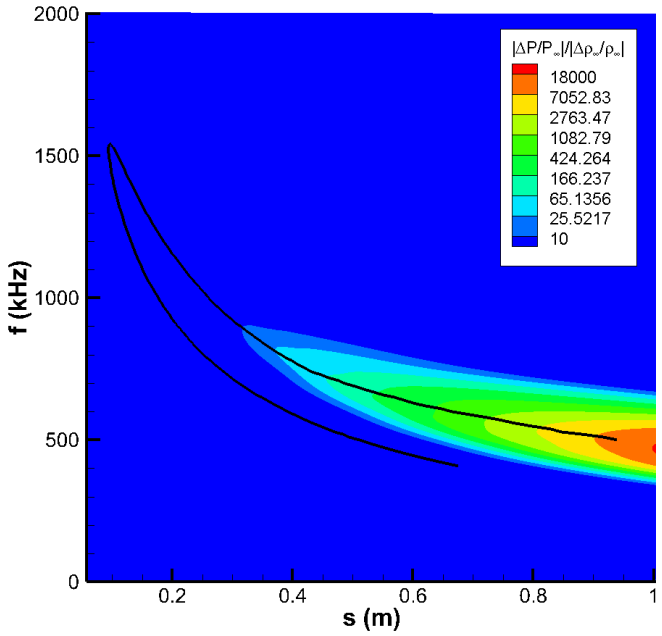

Figure 21. Case 1 Normalized wall-pressure amplitude contours. Black line indicates the LST-derived neutral stability curve. A logarithmic scale is used here to highlight amplitude variations.

the amplitude of the disturbance decays moving downstream. Above $f = 300$ kHz, disturbances undergo oscillatory growth and decay due to forcing. The contour also indicates that the forcing waves created by the shock-disturbance interaction are strongest between $f = 1100$ kHz and $f = 1500$ kHz. The dark red region corresponds to the amplitude attained by the disturbance after the second mode instability and shows that even at high frequencies, the second mode is instability is much stronger than initial excitation by forcing waves.

The normalized wall-pressure amplitude spectra for Case 1 can be seen in more detail in Figure 23. The initial spectrum at s = 0.1 m is smooth in a sense that a large range of frequencies have similar amplitudes. Moving downstream, more and more frequencies enter the second-mode instability region and those frequencies are amplified. A distinctive peak appears in the spectrum, which corresponds to the most amplified second-mode frequency at that streamwise distance. Moving downstream, the peak shifts towards lower frequencies due to the growth of the boundary layer. Simultaneously, the peak itself increases in amplitude because lower frequencies experience more amplification. In addition, the peak frequency changes more slowly with increasing streamwise distance and suggests that the peak frequency will converge onto a single frequency sufficiently far downstream. At s = 1.0 m, the peak is located at $f = 470$ kHz. It is interesting to note that the peak frequency at $s = 1.0$ is very similar to the results obtained by Knisely and Zhong,[3] although they used a blowing/suction slot located on the surface of the cone to perturb the flowfield. This may indicate that the peak frequency does not necessarily depend on the characteristics of the initial disturbance. At $s = 1.0$ m, secondary peak can be seen around $f = 940$ kHz, which corresponds to the first harmonic of the primary peak frequency. At this distance, the disturbance amplitude has grown large enough to excite a nonlinear harmonic frequency. However, this secondary peak is about 3,000 times smaller in amplitude than the primary peak, so the effect of nonlinearity is still quite weak.

The DNS results were also validated with LST. The comparison is presented in Figure 24 for $f = 600$ kHz and provides insight into the receptivity mechanism here. The DNS phase speed (and growth rate) is highly oscillatory upstream because of modulation by the forcing waves. However, this oscillation seems to be centered around a point between the entropy and fast acoustic spectrum, far away from the slow acoustic spectrum. In addition, the oscillation seems to track mode $F1^+$ qualitatively. This suggests that mode $F1^+$ was excited by fast acoustic waves generated by the interaction of the planar entropy pulse with the shock upstream.

Moving further downstream, LST predicts that mode $F1^+$ synchronizes with the entropy/vorticity spectrum around $s = 0.345$ m. The DNS results also indicate a local region of growth around the same lo-

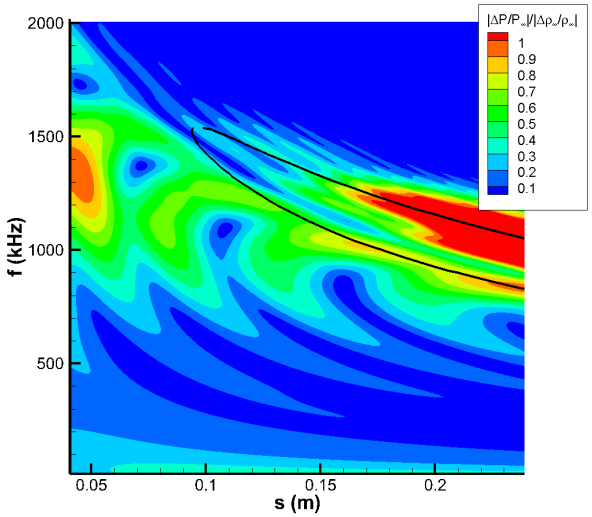

Figure 22. Case 1 normalized amplitude contours in upstream region. Contours are rescaled to highlight excitation due to forcing waves. Black line indicates the LST-derived neutral stability curve.

cation. Fedorov and Khokhlov[38] have shown that mode F1 can be excited through synchronization with entropy/vorticity waves. In other words, this growth is probably due to a resonant interaction between mode $F1^+$ and the entropy forcing waves around this location. Further downstream, around $s = 0.48$ m, mode $F1^+$ reaches its peak growth rate, and the DNS phase speed starts to agree well with the mode $F1^+$ phase speed. This suggests that mode $F1^+$ dominates the overall disturbance at this location. However, the DNS growth rate is still higher than the LST mode $F1^+$ growth rate. The discrepancy here could be due to the nonparallel effect neglected in LST, as suggested by Knisely and Zhong.[3] Further downstream, when mode $F1^+$ becomes a coalesces with the continuous spectrum, the DNS phase speed instead follows the new mode $F1^-$. Note that the DNS has also predicted an unstable supersonic mode, as indicated by the "kink" in the growth rate curve around $s = 0.63$ m. However, there is a noticeable difference in the length of the supersonic mode region. Although LST predicts the branch II neutral point to be located around $s = 0.66$ m, the DNS neutral point is located around $s = 0.84$ m.

One objective of this study is to obtain receptivity coefficients for the second mode. Here we use the method developed by Huang and Zhong,[39] where the receptivity coefficient of a specific mode and frequency is the ratio of the amplitude of the mode at the branch I neutral point to the amplitude of the initial freestream perturbation. Therefore, the receptivity coefficient at a particular frequency is the normalized amplitude of the mode evaluated at the branch I neutral point for that frequency:

$$C_{rec}(f) = \left.\frac{|\Delta P(f)/P_\infty|}{|\Delta\rho_\infty(f)/\rho_\infty|}\right|_I \tag{18}$$

Since the disturbance is multimodal, the amplitude obtained from FFT is not necessarily equivalent to the amplitude of the second mode itself. However, the amplitude of the second mode can be isolated from the overall disturbance amplitude by using the LST-derived N-factors[37] of the second mode. Since the N-factor represents the ratio of the second mode amplitude at a particular streamwise distance to the second mode amplitude at the branch I neutral point, it can be used to estimate the receptivity coefficient at the branch I neutral point:

$$C_{rec}(f) \approx \frac{1}{e^N}\left.\frac{|\Delta P(f)/P_\infty|}{|\Delta\rho_\infty(f)/\rho_\infty|}\right|_s \tag{19}$$

Note that this method is accurate only if the overall disturbance amplitude is roughly equal to the unstable mode amplitude. That is, the unstable mode must be dominant at the sampled streamwise distance. From the DNS results, the second/supersonic mode became the most dominant around the branch II neutral point. Therefore, the branch II neutral point will be used as the sampling location for this study.

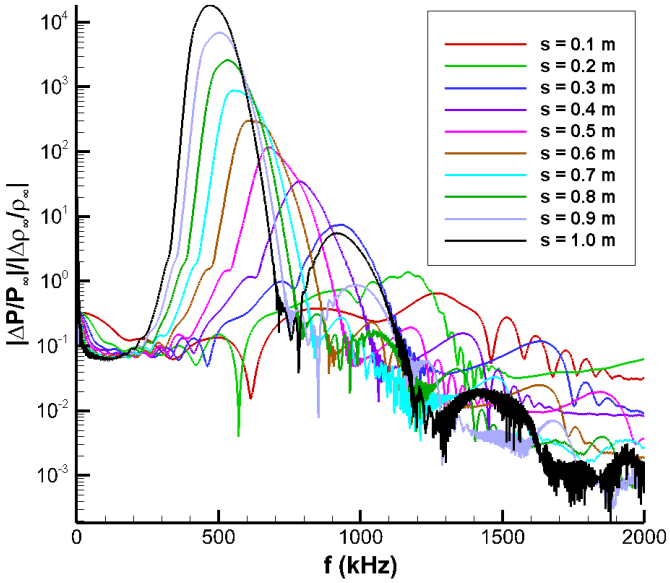

Figure 23. Case 1 Normalized wall-pressure amplitude spectra at various streamwise distances

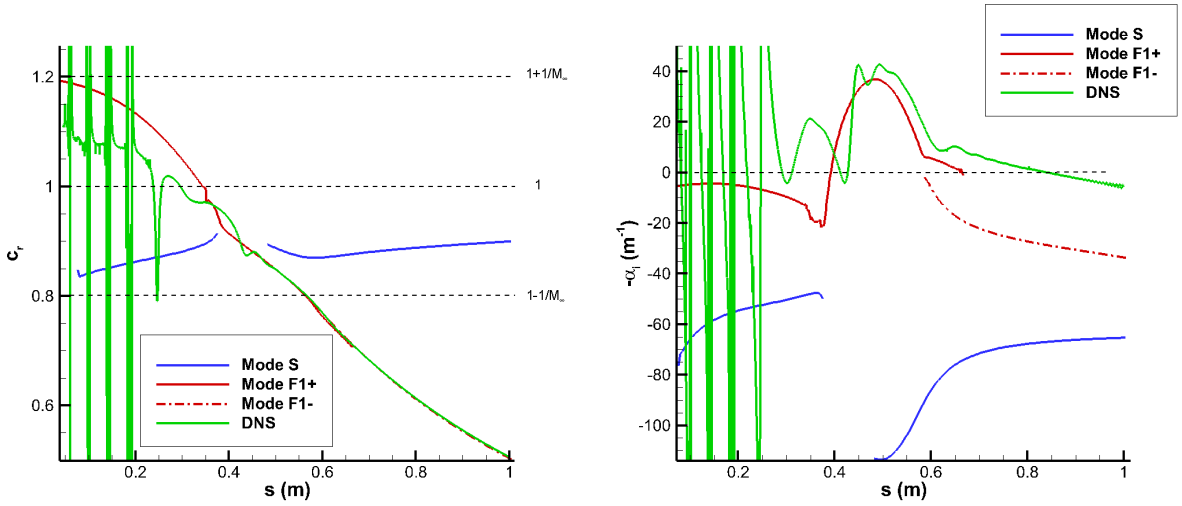

(a) (b)

Figure 24. Case 1 Comparison of phase speed and growth rate between DNS and LST for $f = 600kHz$

Figure 25 presents the receptivity coefficients for the most unstable second-mode frequencies. Overall, it appears that the initial amplitude of the disturbance increases as frequency decreases. There is a "kink" in the receptivity coefficient below $f = 740$ kHz. This may be a result of the extended growth region due to the supersonic mode at lower frequencies. It is interesting to note these coefficients are comparable to the receptivity coefficients obtained by He and Zhong[11] for a planar slow acoustic pulse. In their case, the planar slow acoustic pulse yielded the largest receptivity coefficients compared to planar fast acoustic and entropy pulses. However, the second mode in their case was mode S (the slow acoustic mode). This suggests that even larger receptivity coefficients could potentially be obtained in the current study if the freestream disturbance was a fast acoustic pulse, since the second mode here is mode F1 (a fast acoustic discrete mode). As mentioned earlier, LST seems to under-predict growth rates, possibly due to not accounting for all nonparallel effects. In such cases, a better estimate of the receptivity coefficient of the second mode may be obtained through the parabolized stability equations (PSE) method or a more comprehensive technique such as biorthogonal decomposition.[40]

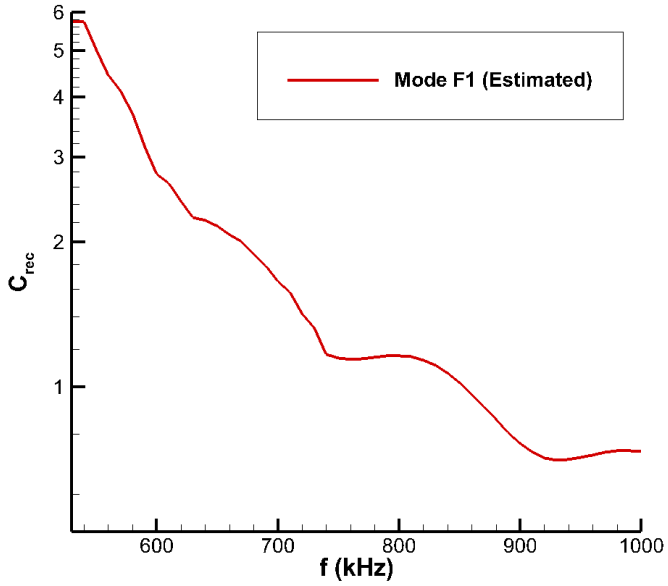

Figure 25. Case 1 Second mode receptivity coefficients obtained through the N-factor estimation method.

B. Case 2 Unsteady DNS Results

The time trace of the wall-pressure disturbance at various upstream locations in Case 2 is presented in Figure 26. The initial wave-packet is similar in shape to the initial wave-packet in Case 1. However, by $s = 0.201$ m, the wave packet has weakened slightly. At $s = 0.400$ m and $s = 0.639$ m the disturbance continues to weaken. Unlike Case 2, the wave packet does not develop a distinct shape. However, it is apparent that the length of the wave packet has increased appreciably.

The normalized wall-pressure amplitude contours presented in Figure 27 confirm the above result. Here, there is no extended region of instability as seen in Case 1. The pressure perturbations are extremely small as well. In addition, the growth regions are very streaky and small in length scale. These growth regions are most likely due to forcing from the waves generated by the shock-disturbance interaction near the nose region. Its clear that beyond $s = 0.4$ m, the amplitude of all sampled frequencies gradually decreases in an oscillatory manner. Because of the absence of the second mode region here, nose bluntness has effectively stabilized the boundary layer. The start of the second mode region is expected to be even further downstream. Again, this delay in instabilities is due to the existence of the entropy layer, which reduces the local Reynolds number.

Figure 28 presents the normalized wall-pressure amplitude of the disturbance at various streamwise locations. The spectrum appears extremely oscillatory compared to Case 1 due to forcing waves and the absence of the second mode. Initially, the spectrum has no clear peak and there are multiple frequencies

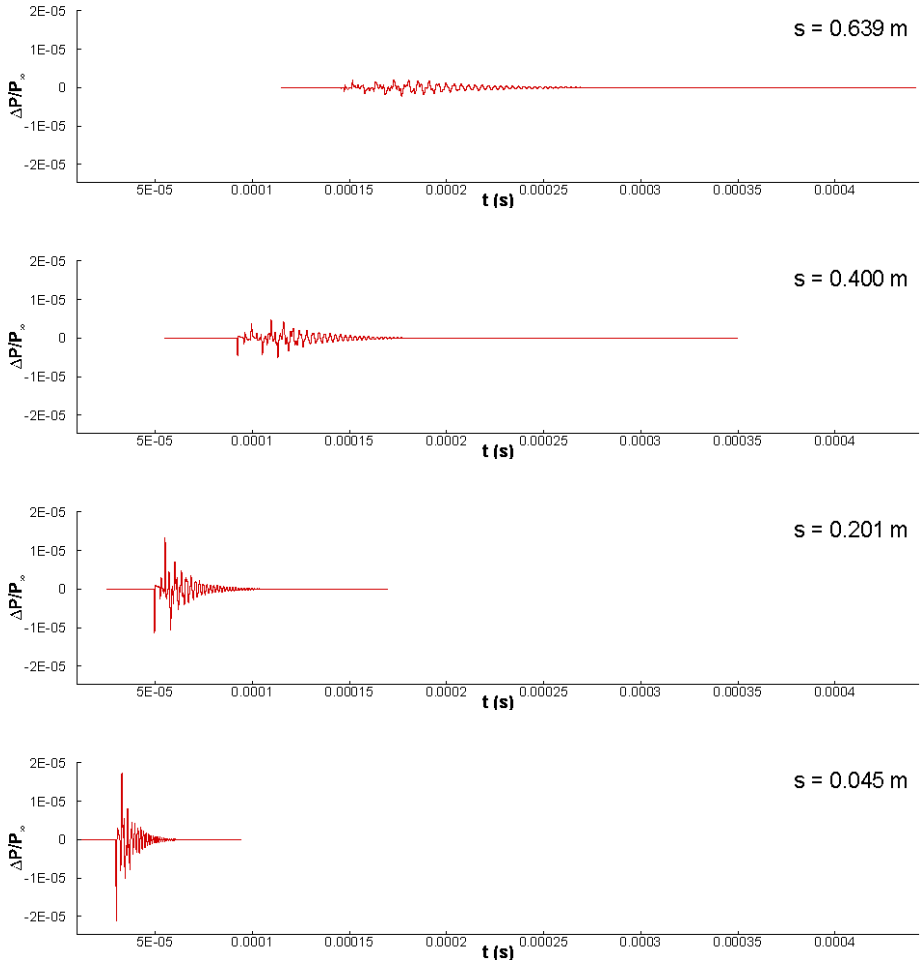

Figure 26. Case 2 Time trace of wall-pressure disturbance at various upstream streamwise distances

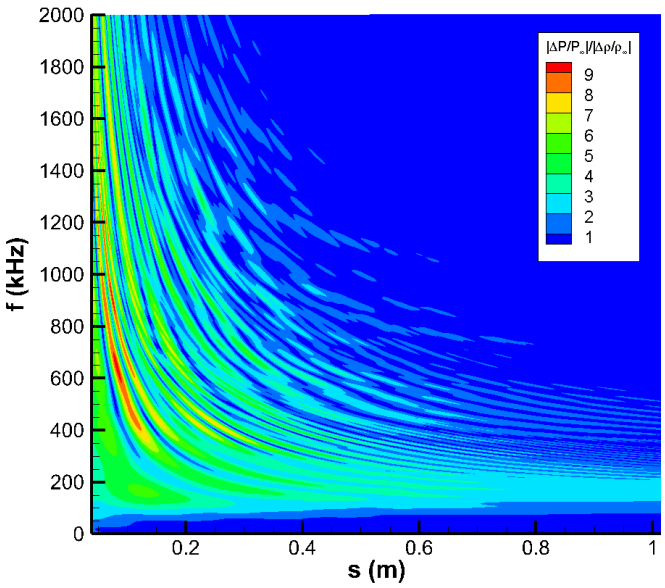

Figure 27. Case 2 Normalized wall-pressure amplitude contour

of comparable amplitude. Moving downstream, a peak starts to form at the lower end of the frequency spectrum. However, this peak is much less prominent relative to the other frequencies in comparison to Case 1. Because blunt noses tend to shift unstable frequencies lower due to the entropy layer effect, it may be more prudent to look more closely at the lower frequencies, as in Figure 28b. The peak amplitude is still very small compared to Case 1 and the peak frequency appears to change very little with streamwise location. Overall, the boundary layer seems to be stabilized relative to Case 1; there is no extended region of growth that would typically be associated with the second mode. Again, note that the results of Case 2 are still preliminary and that a more extensive study is planned to further explore the effect of nose bluntness on second mode receptivity.

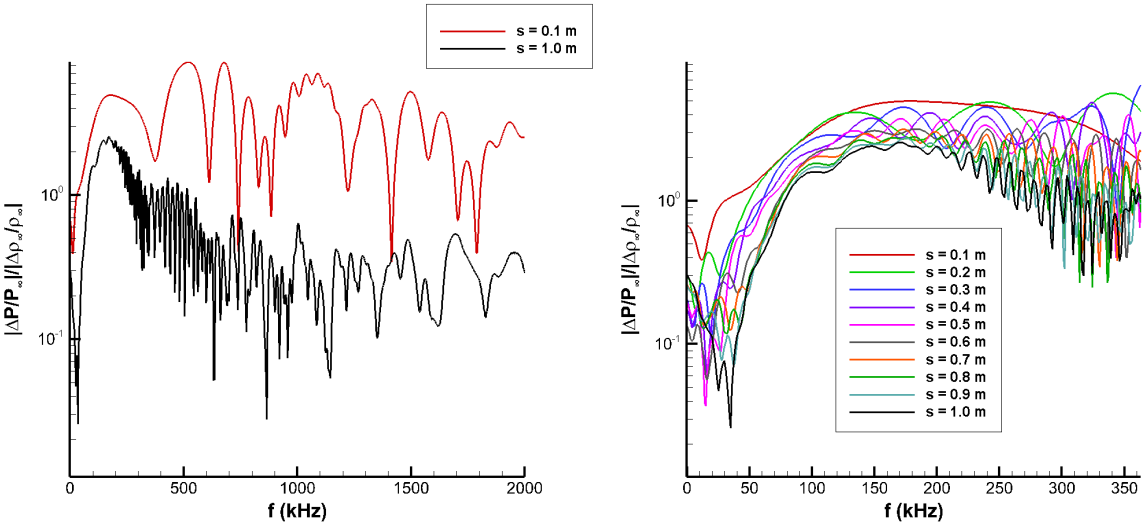

Figure 28. Case 2 (a) Normalized wall-pressure amplitude for full frequency range. (b) Normalized wall-pressure amplitude for lower frequencies

VIII. Conclusion and Future Research

The receptivity of the Mach 5 hypersonic boundary layer over a 5-degree half angle cone with nose radii of 1 mm and 25 mm to a planar entropy pulse was investigated. For both cases, a steady meanflow was converged up to $s = 1.0$ m downstream of the nose using a 5th order thermochemical nonequilibrium DNS code. The steady meanflow was subsequently used as input into thermochemical nonequilibrium LST and as the steady base flow for unsteady DNS, whereby a planar entropy pulse was imposed onto the freestream and the resulting boundary-layer disturbance was tracked as it propagated downstream. FFT was applied to the time trace of pressure perturbations at each streamwise location to obtain amplitude spectra, phase speeds and growth rates at each streamwise location on the cone. The amplitude spectra were then used to obtain receptivity coefficients for the most amplified second mode frequencies using the method of Huang.[37]

In the sharp nose case (Case 1), the second mode was the fast acoustic mode F1 and the second-mode instability region began at a streamwise distance of $s = 0.1$ m. In addition, there was an unstable supersonic mode which extended the instability region for frequencies below $f = 740$ kHz. There was good agreement when comparing the maximum amplitude at any streamwise location in DNS with the neutral stability curves from LST. The phase speed and growth rate obtained from unsteady DNS, when compared with LST, suggested that fast acoustic waves transmitted by the shock-disturbance interaction upstream excited the second mode. In addition, there was a small growth region due to forcing from entropy waves. However, unsteady DNS predicted a longer supersonic mode region than LST. The most-amplified frequency at the end of the cone ($s = 1.0$ m) is $f = 470$ kHz, which matched reasonably well with the LST-derived N-factor curves.

Preliminary receptivity results for the blunt nose case (Case 2) showed that at the streamwise distances simulated (up to $s = 1.0$ m), there was no second mode instability. Therefore the second-mode region appears to have been delayed substantially compared to Case 1. Regardless, there are small regions of growth upstream. However, these growth regions are not expected to be significant owing to their short length scales. The amplitude of the pressure disturbance was seen to decay in amplitude beyond $s = 0.4m$. Despite the absence of the second mode, the amplitude spectra of the disturbance appeared to show a peak frequency.

Future research will build upon the current study in three directions. First, a variety of other freestream pulse disturbances, such as fast acoustic, slow acoustic and vorticity waves will be added in addition to the current case. Second, perfect gas simulations will be performed to better understand the real-gas effect on receptivity. Third, a more extensive study will be conducted on the nose bluntness effect on receptivity.

Acknowledgments

The authors would like to thank Dr. Carleton Knisely for providing the steady meanflow data for Case 1. This research was also partially supported by the AFOSR, under AFOSR Grant #FA9550-19-1-0206, monitored by Dr. Ivett Leyva, and by Office of Naval Research (ONR) Grant #N00014-17-1-2343, currently monitored by Dr. Eric Marineau and previously by Dr. Knox Millsaps. Primary computational resources were provided by Extreme Science and Engineering Discovery Environment (XSEDE) through the Texas Advanced Computing Center (TACC) and San Diego Supercomputer Center (SDSC) under grant number TG-ASC090076, supported in part by the National Science Foundation. Additional computational support was provided by the Department of Defense High Performance Computing Modernization Program (DoD HPCMP) through project AFOSR40702004. The views and conclusions contained herein are those of the authors and should not be interpreted as necessarily representing the official policies or endorsements, either expressed or implied, of the U.S. Air Force Office of Scientific Research, Office of Naval Research, or the U.S. Government.

References

[1]Fedorov, A. and Tumin, A., "High-speed boundary-layer instability: old terminology and a new framework," *AIAA Journal*, Vol. 49, No. 8, 2011, pp. 1647–1657.

[2]Knisely, C. and Zhong, X., "Sound radiation by supersonic unstable modes in hypersonic blunt cone boundary layers. II. Linear stability theory." *Physics of Fluids*, Vol. 31, 2019.

[3]Knisely, C. and Zhong, X., "Sound radiation by supersonic unstable modes in hypersonic blunt cone boundary layers. II. Direct numerical simulation," *Physics of Fluids*, Vol. 31, 2019.

[4]McKenzie, J. F. and Westphal, K. O., "Interaction of Linear Waves with Oblique Shock Waves," *The Physics of Fluids*, Vol. 11, No. 11, November 1968.

[5]Ma, Y. and Zhong, X., "Receptivity of a supersonic boundary layer over a flat plate. Part 2. Receptivity to free-stream sound," *Journal of Fluid Mechanics*, Vol. 488, 2003, pp. 79–121.

[6]Ma, Y. and Zhong, X., "Receptivity of a supersonic boundary layer over a flat plate. Part 3. Effects of different types of free-stream disturbances," *Journal of Fluid Mechanics*, Vol. 532, 2003, pp. 63–109.

[7]Ma, Y. and Zhong, X., "Receptivity of a supersonic boundary layer over a flat plate. Part 1. Wave structures and interactions," *Journal of Fluid Mechanics*, Vol. 488, 2003, pp. 31–78.

[8]Balakumar, P. and Kegerise, M., "Receptivity of Hypersonic Boundary Layers to Acoustic and Vortical Disturbances," *49th AIAA Aerosciences Meeting*, January 2011.

[9]Fedorov, A., Ryzhov, A., Soudakov, V., and Utyuzhnikov, S., "Receptivity of a high-speed boundary layer to temperature spottiness," *Journal of Fluid Mechanics*, Vol. 722, 2013, pp. 533–553.

[10]Huang, Y. and Zhong, X., "Parametric Study of Boundary-Layer Receptivity to Freestream Hot-Spot Perturbation over a Blunt Compression Cone," *AIAA 2014-0774*, 2014.

[11]He, S. and Zhong, X., "Hypersonic Boundary Layer Receptivity over a Blunt Cone to Freestream Pulse Disturbances," *AIAA Scitech 2020 Forum*, , No. AIAA 2020-2057, 2012.

[12]Stetson, K. F., Thompson, E. R., Donaldson, J. C., and Siler., L. G., "Laminar boundary layer stability experiments on a cone at mach 8. part 1: Sharp cone." *AIAA 83-1761*, 1983.

[13]Malik, M. R., Spall, R., and C-L., C., "Effect of Nose Bluntness on Boundary Layer Stability and Transition," *AIAA 90-0112*, 1990.

[14]Lei, J. and Zhong, X., "Linear Stability Analysis of Nose Bluntness Effects on Hypersonic Boundary Layer Transition," *Journal of Spacecraft and Rockets*, Vol. 49, No. 1, 2012.

[15]Kara, K., Balakumar, P., and Kandil, O., "Effects of Nose Bluntness on Hypersonic Boundary-Layer Receptivity and Stability over Cones," *AIAA Journal*, Vol. 49, No. 12, 2011.

[16]Malik, M. R., "Hypersonic flight transition data analysis using parabolized stability equations with chemistry effects," *Journal of Spacecraft and Rockets*, Vol. 40, No. 3, 2003, pp. 332–344.

[17]Chang, C.-L., Vinh, H., and Malik, M., "Hypersonic Boundary-Layer Stability with Chemical Reactions using PSE," *28th AIAA Fluid Dynamics Conference, Snowmass Village, CO, U.S.A.*, 1997.

[18]Johnson, H. B., Seipp, T. G., and Candler, G., "Numerical study of hypersonic reacting boundary layer transition on cones," *Physics of Fluids*, Vol. 10, No. 10, 1998, pp. 2676–2685.

[19]Johnson, H. B. and Candler, G., "Hypersonic Boundary Layer Stability Analysis Using PSE-Chem," *AIAA 2005-5023*, 2005.

[20]Johnson, H. B. and Candler, G., "Analysis of Laminar-Turbulent Transition in Hypersonic Flight Using PSE-Chem," *AIAA 2006-3057*, 2006.

[21]Hudson, M. L., Chokani, N., and Candler, G., "Linear Stability of Hypersonic Flow in Thermochemical Nonequilibrium," *AIAA Journal*, Vol. 35, No. 6, 1997, pp. 958–964.

[22]Mortensen, C., "Toward an understanding of supersonic modes in boundary-alyer transition for hypersonic flow over blunt cones," *Journal of Fluid Mechanics*, Vol. 846, 2018, pp. 789–814.

[23]Knisely, C. and Zhong, X., "Impact of Vibrational Nonequilibrium on the Supersonic Mode in Hypersonic Boundary Layers," *AIAA Journal*, Vol. 58, No. 4, 2020.

[24]Ma, Y. and Zhong, X., "Numerical Simulation of Receptivity and Stability of Nonequilibrium Reacting Hypersonic Boundary Layers," *39th Aerospace Sciences Meeting*, , No. AIAA 2001-0892, 2001.

[25]Parsons, N., Zhong, X., Kim, J., and Eldredge, J., "Numerical Study of Hypersonic Receptivity with Thermochemical Non-Equilibrium on a Blunt Cone," *AIAA 2010-4446*, 2010.

[26]Bitter, N. and Shepherd, J., "Stability of highly cooled hypervelocity boundary layers," *Journal of Fluid Mechanics*, Vol. 778, 2015, pp. 586–620.

[27]Mortensen, C. H. and Zhong, X., "High-Order Shock-Fitting Method for Hypersonic Flow with Graphite Ablation and Boundary Layer Stability," *AIAA 2012-3150*, 2012.

[28]Mortensen, C. H. and Zhong, X., "Numerical Simulation of Graphite Ablation Induced Outgassing Effects on Hypersonic Boundary Layer Receptivity over a Cone Frustum," *AIAA 2013-0522*, 2013.

[29]Mortensen, C. H. and Zhong, X., "Real Gas and Surface Ablation Effects on Hypersonic Boundary Layer Instability over a Blunt Cone," *AIAA 2013-2981*, 2013.

[30]Mortensen, C. H. and Zhong, X., "Simulation of Second-Mode Instability in a Real-Gas Hypersonic Flow with Graphite Ablation," *AIAA Journal*, Vol. 52, No. 8, 2014, pp. 1632–1652.

[31]Mortensen, C. H. and Zhong, X., "Numerical Simulation of Hypersonic Boundary-Layer Instability in a Real Gas with Two-Dimensional Surface Roughness," *AIAA 2015-3077*, 2015.

[32]Mortensen, C. H., *Effects of Thermochemical Nonequilibrium on Hypersonic Boundary-Layer Instability in the Presence of Surface Ablation and Isolated Two-Dimensional Roughness*, Ph.D. thesis, University of California Los Angeles, 2015.

[33]Zhong, X., "High-Order Finite-Difference Schemes for Numerical Simulation of Hypersonic Boundary-Layer Transition," *Journal of Computational Physics*, Vol. 144, No. 2, 1998, pp. 662–709.

[34]Liu, Y. and Vinokur, M., "Nonequilibrium Flow Computations. I. An Analysis of Numerical Formulations of Conservation Laws," *Journal of Computational Physics*, Vol. 83, No. 2, 1989, pp. 373–397.

[35]Prakash, A., Parsons, N., Wang, X., and Zhong, X., "High-order Shock-fitting Methods for Direct Numerical Simulation of Hypersonic Flow with Chemical and Thermal Nonequilibrium," *Journal of Computational Physics*, Vol. 230, No. 23, 2011, pp. 8474–8507.

[36]Knisely, C. and Zhong, X., "An Investigation of Sound Radiation by Supersonic Unstable Modes in Hypersonic Boundary Layers," *AIAA 2017-4516*, 2017.

[37]Huang, Y., *Numerical Study of Hypersonic Boundary-Layer Receptivity and Stability with Freestream Hotspot Perturbations*, Ph.D. thesis, University of California Los Angeles, 2016.

[38]Fedorov, A. and Khokhlov, A., "Prehistory of Instability in a Hypersonic Boundary Layer," *Theoretical Computational Fluid Dynamics*, Vol. 14, No. 6, 2001, pp. 359–375.

[39]Huang, Y. and Zhong, X., "Numerical Study of Laser-Spot Effects on Boundary-Layer Receptivity for Blunt Compression-Cones in Mach-6 Freestream," *AIAA 2010-4447*, 2010.

[40]Miselis, M., Huang, Y., and Zhong, X., "Modal Analysis of Receptivity Mechanisms for a Freestream Hot-Spot Perturbation on a Blunt Compression-Cone Boundary Layer," *AIAA 2016-3345*, 2016.